Detonation performance experiments and modeling for the DAAF-based high explosive PBX 9701

Carlos Chiquete*, Scott I. Jackson, Eric K. Anderson, Mark Short

Los Alamos National Laboratory
Los Alamos, NM 87545 USA

Abstract

Detonation performance experiments and modeling are reported for the explosive PBX 9701, which is composed of 97% 3,3'-diamino-4,4'-azoxyfurazan (DAAF) and 3% vinylidene fluoride-chlorotrifluoroethylene copolymer (Kel-F 800) binder by weight. PBX 9701 is a newly-developed reduced-sensitivity explosive with increased performance relative to the triaminotrinitrobenzene or TATB-based PBX 9502 while still retaining low sensitivity to mechanical insult. The first detonation performance measurements for this formulation are presented, including front-curvature rate sticks and cylinder expansion test data. Prior shock initiation data is also reviewed. These data are used to develop programmed burn (PB) and reactive burn (RB) calibrations for existing commonly-used performance models which allow engineering calculations with PBX 9701. The calibration process involves several enhancements relative to conventional approaches including the use of an analytical scaling correlation to speed the equation of state (EOS) calibration process which uses a PB hydrocode-based approach and development of a new methodology to improve the consistency between the PB and RB model calibrations and associated calculations. This link is achieved by populating the RB products EOS in direct reference to the PB release isentrope and Chapman-Jouguet state and in calibrating the timing components of each model using an equivalent procedure, all in order to facilitate comparison between the two modeling approaches. Overall, PBX 9701 is seen to exhibit improved performance relative to insensitive explosives, with a trinitrotoluene (TNT) equivalence of 1.24. The detonation performance properties are found to be well captured by existing

*Corresponding author
Email address: chiquete@lanl.gov (Carlos Chiquete)

models.

Keywords: detonation performance, calibration, reactive burn, programmed burn, high explosive

1. Introduction

Explosive formulations used in engineering applications are generally selected for a combination of their explosive performance properties and ability to withstand mechanical and thermal insults. Different balances of these properties are often required for varying needs. Common explosives utilized in high explosive (HE) engineering applications include PBX 9501, which is a high-performing cyclotetramethylene- tetranitramine (HMX)-based formulation, and PBX 9502, which is an insensitive 1,3,5-triamino-2,4,6-trinitro-benzene (TATB)-based formulation. A newly discovered synthesis pathway [1] has renewed interest in DAAF (3,3'-diamino-4,4'-azoxyfurazan), an explosive molecule with comparable mechanical sensitivity to TATB, but with increased detonation performance properties [2] and comparable shock sensitivity to HMX.

In this work, we characterize the detonation performance properties of PBX 9701, a plastic-bonded explosive formulation that is composed of 97% DAAF and 3% Kel-F 800 (vinylidene fluoride-chlorotrifluoroethylene copolymer) plasticizer. Explosive performance test data is reported including rate stick data for three charge-diameters to measure both detonation speed and front shape and a copper cylinder expansion test to capture the ability of the explosive to push metal. This combination of data sets has previously proven reliable in producing predictive performance models for a variety of explosives. The obtained data are used to yield calibrations for the Detonation Shock Dynamics (DSD) [3–5] propagation model, the Jones-Wilkins-Lee (JWL) product equation-of-state (EOS) model, and the Wescott-Stewart-Davis (WSD) model [6]. Also examined are the diameter-effect curve and product energy for PBX 9701 relative to the more common PBX 9501 and PBX 9502 explosives.

1.1. Prior DAAF Performance Work

Detonation performance data characterizes both the timing and metal push capability of a detonating explosive. Timing refers to the time the wave arrives at each location in a charge. Push refers to the ability of the detonation products to perform work on adjacent materials. In a review paper, Koch [2] documents some preliminary performance characteristics of early DAAF-based formulations

(including PBX 9701, then known provisionally as LAX-133) including detonation velocity (for a single diameter), predicted Chapman-Jouguet detonation conditions, and their variation with initial density. The related shock initiation properties are also discussed. Tappan et al. [7] characterizes the metal pushing characteristics of several DAAF formulations, but not PBX 9701. Chavez et al. [8] reports cylinder expansion and wedge tests for a similar formulation (95% DAAF, 5% Kel-F 800), but using older streak-camera based diagnostics. Ramos et al. [9] has also used embedded gauges to characterize this PBX 9701 initiation properties, finding similar results to those presented in Koch [2]. This limited amount of performance data, including a single rate stick at the explosive's nominal density and no front curvature measurement, serves as the major motivation for this current work. Typically, a variety of charge sizes are used to characterize the diameter effect on phase speed and front curvature for a given HE and therefore properly constrain the subsequent modeling and calibration of the data. Additionally, no cylinder expansion test had been performed using the specific PBX 9701 formulation, making this an additional, essential objective of our work.

1.2. Modeling Approaches

Detonation of condensed-phase explosives involves the convolution of solid mechanics, chemical reaction kinetics, and compressible fluid mechanics. Modeling the combined complexity of these processes in a detailed fashion at engineering scales is beyond current model and computational capabilities, and detonation modeling instead relies on approximate and empirical subscale techniques. Two different methodologies are commonly used at engineering scales for detonation performance modeling in practice and are referred to as programmed burn (PB) and reactive burn (RB) models. Engineering scales are typically several orders of magnitude larger than the RZ length and time scales. Both approaches require experimental data for calibration.

Reactive burn models approximate the detonation process via a conversion of a reactant state to a product state governed by a finite reaction rate. These models require four components, a reactant EOS, a product EOS, a reaction rate term, and a thermodynamic closure condition between the reactant and product phases. Generally, each of these components have semi-analytical empirical forms due to the difficulties in measuring the extreme conditions and short timescales associated with the HE detonation process. Commonly adopted RB models for high explosives include the Ignition and Growth and WSD (Wescott-Stewart-Davis) models [6, 10]. RB models are able to resolve the spatially finite reaction zone

(RZ), which is modeled as a mixture of the reactant and product states. This feature can be appealing when the interaction of the reaction zone with other parts of the flow, such as confiners, is relevant. However, the reaction zone length scales are typically small relative to the scale of the simulation, which can result in significant computational expense even when using simplified RB models. For many calculations, stringent resolution requirements may render resolved calculations intractable, necessitating approaches requiring less computational expense.

Programmed burn models separately calculate the temporal detonation evolution from the subsequent energy release for improved computational efficiency. Such models approximate the detonation as a shock front followed by a product field with an infinitely thin reaction zone particularly for explosive design calculations. Thus, these models consist of two components. The first is a shock propagation law, which is used to predict how the detonation front shape and motion evolves as a function of time and space. The second is a product state with a defined EOS that is active immediately behind the shock front to do work on surrounding material. The shock propagation law can be as simple as Huygens construction (constant speed of propagation), though in practice the physics-based Detonation Shock Dynamics (DSD) relationship is used. This relates local wave velocity to local curvature on the front with an intrinsic surface evolution law [3–5]. Product EOSs such as the JWL or Davis EOS are commonly used [11–13]. Model enhancements also exist to make these approaches more realistic including a velocity-adjusted JWL method [14, 15] that modulates the product state to the local surface normal speed and a Pseudo-Reaction Zone approach that mimics the main features of a RB model, with the release energy due to reaction occurring over a finite length zone [16].

Most HE performance model calibration studies tend to focus on of these two approaches in isolation. Therefore, there is no guarantee PB and RB models for a given explosive have consistent energy release and propagation or timing information, which can complicate comparisons between PB and RB results. Our goal here is to allow a more transparent evaluation of the relative merits of the two approaches based on the different physics embedded in each model, rather than inconsistencies in how the timing or energy release is set in each calibration process. We attempt to link these dissimilar modeling approaches more explicitly as we standardize the products EOS (which largely sets the metal push) between the methods and also use the same exact process for calibrating the detonation propagation aspect.

In the following sections, we first report on the performance experiments we use to generate our new performance models for PBX 9701. These are compared

to equivalents for PBX 9502, composed of 95% TATB and 5% Kel-F 800 by weight and PBX 9501, composed of 95% HMX and 2.5% Estane and a 2.5% eutectic mixture of bis(2,2-dinitropropyl)acetal and bis(2,2-dinitropropyl)formal (BDNPA/BDNPF) also by weight. Then, we describe the model methodologies and calibration results obtained from the generated data set. The PB and RB model calibrations are then compared in the context of the cylinder expansion test, highlighting common and dissimilar elements.

2. Experiments

The PBX 9701 performance tests consisted of three different diameter two-dimensional (2D) axisymmetric cylindrical, unconfined rate stick tests and one cylinder expansion test. Front-curvature rate sticks are used to experimentally characterize the variation of detonation shape and and velocity with charge scale [17], which is subsequently used to yield a DSD calibration [18] for PB models and also serve as calibration data for RB models [19]. A cylinder expansion tests (CYLEX) is also used to characterize the EOS of the detonation products [20–22]. The experimental details of each test geometry are described below.

2.1. Test Geometries

Table 1: Experimental test type, diameter (d), initial explosive density (ρ_0) which is an average over the individual pellet densities for each test's velocity measurement region, and measured detonation velocity (D_0). "DetV", "FC", and "CYLEX" indicates detonation velocity, front curvature and detonation velocity, and cylinder expansion test, respectively.

Identifier	Type	d (mm)	ρ_e (g/cc)	D_0 (mm/μs)
8-1896	DetV	6.35	1.692	7.854 ± 0.003
8-1897	FC	6.35	1.695	7.863 ± 0.003
8-1895	FC	9.5	1.693	7.879 ± 0.002
8-1887	FC	25.5	1.696	7.936 ± 0.004
8-1905	CYLEX	25.5	1.692	7.925 ± 0.003

The rate stick tests consisted of unconfined cylinders of explosive as shown in Fig. 1. Three different diameters, 6.4, 9.5 mm, and 25.5 mm, were tested with

details as given in Table 1. Each rod was composed of 12 individual explosive pellets and had a total length-to-diameter ratio (L/d) of 12 which has previously been shown to be sufficiently long to generate a steady detonation velocity [17]. Each pellet was uniaxially pressed from molding powder in the shape of a right circular cylinder with an L/d ratio of unity. The total density variation across all pellets per test was ± 0.001 g/cm^3. All pellets were glued together with Angstrom-Bond 9110LV epoxy under pressure to achieve glue joint thicknesses of less than 10 μm. Individual pellet densities were chosen to be as similar as possible with

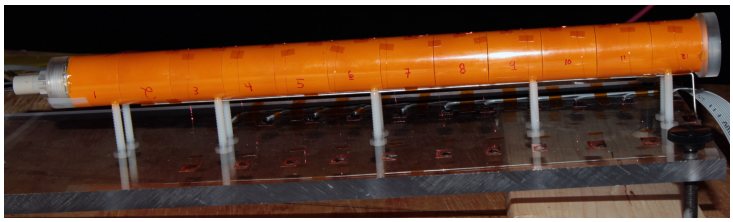

Figure 1: Front-curvature rate stick 8-1887 with the detonator at left and the break-out window on the right.

the pellets ordered with increasing density from the detonator end. The specific pellet densities as measured with an immersion densitometer are shown in Table 1. Each rate stick was minimally supported (Fig. 1) to avoid confining the detonation reaction zone. The PBX 9701 pellets were initiated directly from a Teledyne RISI RP-1 detonator for all tests and equipped with both ionization probes and front shape mirrors as described below.

The cylinder expansion test consisted of an inert confiner tube tightly encasing a rod of PBX 9701 explosive, as shown in Fig. 2. The tube was composed of Oxygen-Free High-Conductivity (OFHC) copper annealed to a dead-soft temper. The test scale was a standard 1-inch cylinder test [23] with an outer diameter of 30.5 mm, an inner diameter of 25.5 mm, a wall thickness of 2.5 mm, and a length of 305 mm. Twelve explosive pellets of PBX 9701 with an outer diameter of 25.5 mm and an L/d of unity were inserted into the cylinder to fully fill it. Pellet joints and the small gap between the cylinder inner diameter and the explosive were filled with Sylgard 184 silicone elastomer to secure the explosive and prevent jetting. Individual pellet densities were similar and are shown in Table 1. Four collimated PDV probes were used to measure the motion of the wall during the experiment. The PDV probes were oriented normal to the initial cylinder wall orientation to generate the most direct measurement of the wall motion [24] for subsequent analysis. Probes were located at two different axial distances from the

detonator–explosive interface, specifically at 152 mm and 203 mm. Each probe was placed at a different azimuthal location, 90 degrees apart as shown in Fig. 2. In similar fashion to the rate stick tests, the cylinder test was directly initiated from a Teledyne RISI RP-1 detonator and equipped with both shorting wires and a front shape mirror as described below.

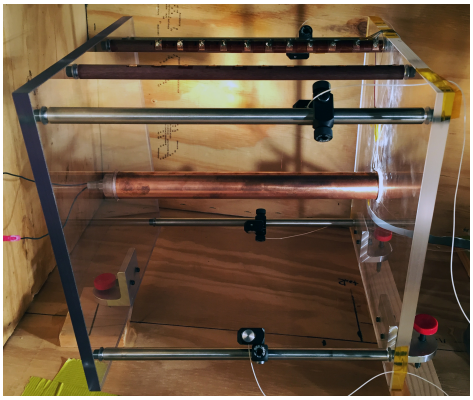

Figure 2: Cylinder test 8-1905 with the detonator at left, breakout window at right.

2.2. Diagnostics

Ionization probes, as described in [17], were used to characterize the detonation phase velocity D_0 at the rate stick outer radius. Each rate stick was instrumented with 11 ionization probes. The cylinder test was similarly instrumented, however the probes were set up to operate as shorting wires for this test as they transmitted current to the tube (acting as a ground as described below) instead of through the detonation reaction zone. The first probe was located at an axial distance of $2d$ from the detonator–explosive interface. The other probes were equidistantly spaced over the remaining $10d$, resulting in a probe separation spacings of $0.909d$. Each probe consisted of a 50.2-μm-diameter (44-AWG) coated copper magnet wire bent into a chevron shape, with the tip located along a line parallel to the axial charge centerline so that the detonation would first contact this tip. Each wire was raised to an electrical potential of 75.0 V through use of an RC circuit. For rate sticks, a single, thicker copper grounding wire was located on a line parallel to the axial centerline of the opposing charge surface. For the cylinder test, the copper tube served as the ground. Arrival of the ionization front associated with the detonation wave at each probe vaporized the thin enamel coating and allowed current to flow from the high-voltage wire to ground, resulting in

a measured voltage drop across the resistor in the RC circuit. Similarly, for the cylinder test, the arrival of the incident shock at the cylinder wall allowed for the insulated wire to short to the wall, generating current flow. Probe locations were measured to better than 30 μm and the pin voltage was sampled with a bandwidth of 1 GHz (5 GS/s sample rate) during each test. Probe position and detonation arrival time data were fitted to a line using a least-squares fit optimization. The slope of the line was the steady-state detonation velocity D_0. These velocities are reported in Table 2 along with the standard error (SE) associated with the fit to D_0.

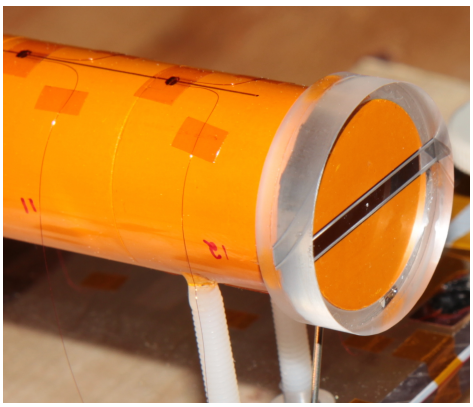

Figure 3: The window on the breakout surface of test 8-1887.

The detonation front shape was recorded at the breakout surface of the downstream pellet using a mirror destruction technique [25]. A PMMA window was glued over the downstream pellet face and a diameter chord of the window was coated with an order-one-μm-thick aluminum layer (Fig. 3). During the experiment, light was directed from an argon flash [26] to this aluminum layer (Fig . 4). That light was then specularly reflected to a Cordin 131 streak camera. Arrival of the detonation at the downstream face destroyed the aluminum surface and cut off the reflected light, allowing the shape of the detonation to be recorded at the breakout face.

The PDV probes used for the cylinder test were collimated with a 100-mm working distance and a spot size of less than 350 μm. Each probe was located approximately 150 mm from the initial cylinder wall location. The portion of the cylinder wall that was observed by each probe was sanded with 600-grit sandpaper to generate diffuse reflectivity. PDV data was recorded at a bandwidth of 20 GHz (50 GS/s digitizer rate) and reduced using a 32-bit Fourier window size and a

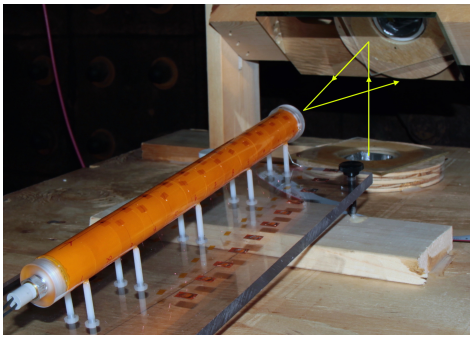

Figure 4: The light path from the argon flash (inset into the test table) to the rate stick window to the streak camera (off image, to the right) for test 8-1887.

4096-bit window step size.

2.3. Experimental Results

2.3.1. Detonation Velocity Reduction and Trends

An example of the ionization wire data is shown in Fig. 5a. The arrival of the detonation allows the voltage to short through the reaction zone and gives a sharp spike in the voltage differential across the resistor in the RC circuit. Trigger times are identified as the time that each voltage trace is elevated above a threshold voltage, which is 1.2V for the case shown.

Probe position (x) and detonation arrival time data (t) were fitted to a line ($x = D_0\,t + x_0$) using a least-squares fit optimization for the parameters D_0 and x_0 as shown in Fig. 5b. The slope of the line was the steady-state detonation velocity D_0. These velocities are reported for each test in Table 1 along with the $\pm$ standard error (SE) associated with the fit to D_0. The fits were excellent in the present study with standard errors less than 0.05%, indicating that the detonation was extremely steady over the region of the rate stick that was equipped with wires. In practice, we have found that standard errors near 0.5-1% are more indicative of highly unsteady detonation in the rate stick geometry. For example, a previous work [27] characterized the velocity across a rate stick composed of alternately stacked explosive pellets of differing formulation and detonation velocity ranging from 6.6-8.5 mm/μs. A linear fit to the ionization wires used in that experiment [27] yields D_0 = 7.462 $\pm$ 0.086, which is a standard error of 1.15%.

Figure 6a shows the diameter-effect, or velocity variation with inverse diameter, trend produced from the rate stick tests. An Eyring form fit to the data is

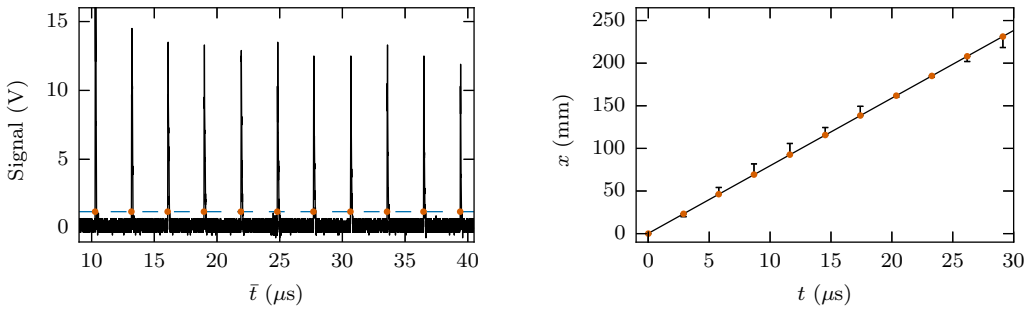

(a) (b)

Figure 5: (a) The ionization wires signal for test 8-1887 plotted as function for absolute or test time ($\bar{t}$). The black trace is the measured voltage; the dashed line is the threshold voltage value; and the dots are the trigger time for each wire. (b) The fit of $x = D_0\, t + x_0$ to the position-time ionization wires data for test 8-1887 (where t is the time from the first triggered probe), yielding D_0 = 7.936 $\pm$ 0.004 and x_0 = 0.273 $\pm$ 0.073. Bars indicate the 100 $\times$ the difference between the data and the fit prediction for each point.

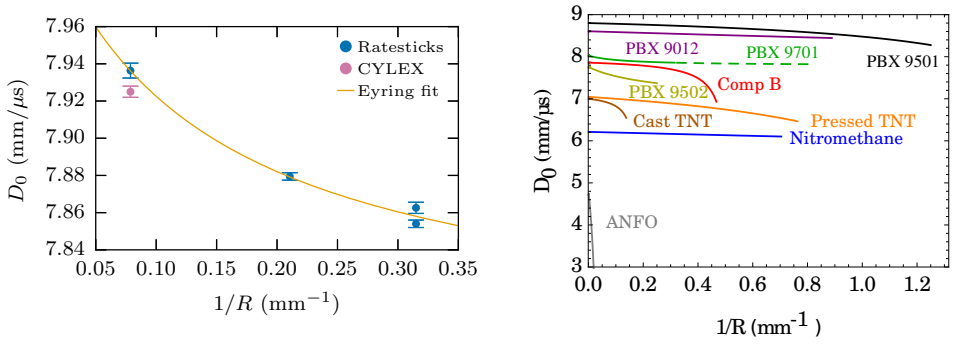

(a) (b)

Figure 6: (a) Diameter effect for PBX 9701 with experimental error bars. (b) Diameter effect trend for PBX 9701 relative to other explosives. Solid line indicates measured range, while dashed line is extrapolated to the anticipated failure diameter range [2].

produced from

$$D_0(\ell) = D_\infty \left(1 - \frac{A}{\ell - R_1}\right), \tag{1}$$

with D_∞ = 8.026 mm/μs, A = 0.2291 mm, R_1 = -7.771 mm and ℓ is the charge-radius. The curve is convex relative to the origin, which is relatively atypical for most explosives [28] but has been seen to occur for insensitive explosives like PBX 9502, where multiple reaction rates are dominant at different scales [17]. Subsequent modeling analysis appears to support this trend as well. Note that the CYLEX velocity is marginally lower than the corresponding rate stick, probably owing to differences in initial density for the two tests.

Figure 6b compares the diameter effect of PBX 9701 to several other explosives. On such a plot, trajectories with smaller slopes are are indicative of more ideal detonation performance, as D_0 does not significantly vary with charge size. The trajectory of PBX 9701 is seen to be quite ideal and similar to PBX 9501 and nitromethane. PBX 9701 is also seen to detonate at a faster velocity and at smaller diameters relative to PBX 9502.

2.3.2. Front Shape Reduction and Trends

The detonation front shapes were recorded on the streak camera film. Each record was digitized by scanning it at 6400 dots per inch. The fronts were then manually detected and scaled using fiducials present during testing to yield the front shape points as shown in Fig. 7b (after a small linear tilt-correction). Each reported front shape consisted of approximately 120 points.

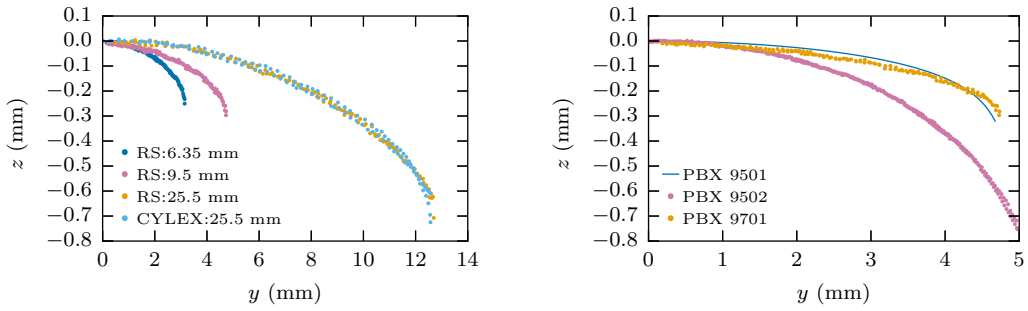

(a) (b)

Figure 7: (a) Front shape measurements. (b) Front shape records for PBX 9701 and 9502 [29] at diameters of 9.5 and 10.0 mm, respectively. A PBX 9501 DSD-calculated front shape also appears for a 9.5 mm diameter rate stick.

The measured fronts for the unconfined PBX 9701 rate sticks are shown in Fig. 7a. Qualitatively, they show increased height variation with increasing diameter,

which is a common trend. The front shape from the CYLEX test and the 25.5 mm unconfined rate stick are nearly identical, indicating that the detonation in the CYLEX test did not experience significant confinement due to the thickness of the Sylgard layer. Figure 7b compares the measured front shape at similar charge-diameters for PBX 9701 and PBX 9502, and a DSD calculation for PBX 9501 [30] as an equivalent experimental measurement is not available at a similar charge radius. The observed front deflection for PBX 9701 is evidently much smaller than its equivalent for PBX 9502. In contrast, the PBX 9701 front variation is comparable to PBX 9501.

2.3.3. CYLEX Wall Velocimetry and Trends

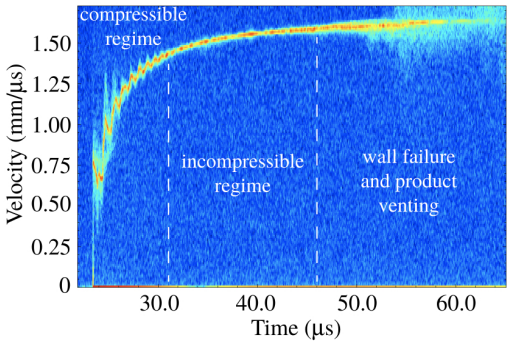

Figure 8: The velocity spectrogram for probe PDV1.

Figure 8 shows a velocity spectrogram obtained from a PDV probe for the single CYLEX test. All probe profiles exhibit characteristically similar features. The detonation is supersonic relative to the sound speed of the copper tube and drives a shock wave into the wall upon arriving at the probe location, rapidly accelerating the radial speed component to 0.77 mm/μs. The detonation products are then at sufficiently high pressure to accelerate the wall in a compressible fashion, resulting in oscillatory motion for several microseconds. This "ring-up" behavior is due to the passage of an alternating series of shocks and rarefactions through the copper, which equilibrate the pressure across the inner and outer wall surfaces. The amplitude of the ringing oscillations decreases over time as the cylinder expansion decreases the product gas pressure until the motion becomes incompressible, resulting in smooth acceleration after about 8 μs when the wall is moving at 1.45 mm/μs. The wall then continues to smoothly accelerate to about 1.58 mm/μs until failing after 20 μs of motion, as indicated by the large velocity spread associated with product venting and wall failure. The normal wall velocity time profile

is generated from this signal by extracting the strongest velocity signal for each time.

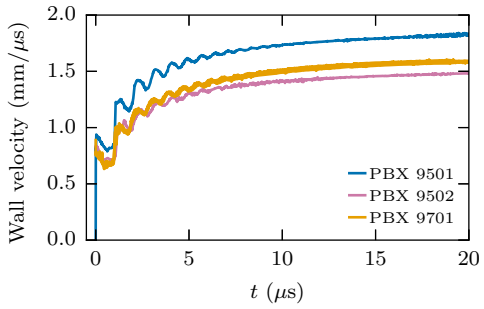

Figure 9: CYLEX wall velocity profiles for the present PBX 9701 test (all probes) and prior PBX 9501 and PBX 9502 tests [31, 32]. Results plotted as function of time (t) relative to wave arrival.

The resulting velocity signal is shown in Fig. 9. For comparison, the wall motion obtained by Pemberton et al. [31, 32] for PBX 9501 and 9502 are also shown in Fig. 9, situating PBX 9701 as a midpoint in terms of the energy delivered to the copper wall. Therefore, the experimental results indicate that PBX 9701 has the features of an insensitive explosive (most prominently in its diameter effect), but detonates in a more ideal and energetic manner than its TATB-based counterpart PBX 9502.

3. Model calibration

In this section, the experimental data is used to parameterize both a reactive burn and a programmed burn model for PBX 9701. The reactive burn model used is the WSD model [6]. The programmed burn model is composed of a DSD propagation law and a Velocity-Adjusted JWL (VAJWL) equation of state model for the products. The approach utilized here links these two models together through the products EOS and detonation timing aspect of the calibration of each method in a novel way to ensure consistency between the PB and RB models. This allows users to explore the relative capabilities of each model when applied to a common geometry and to use either model methodology as needed depending on the physical and computational requirements of their problem. It should be noted that the two methods encode very different physics, especially in regards to initiation.

Many detonation phenomena such as dead zones or desensitization for example are well beyond the predictive scope of PB methods.

The calibration process is as follows. First, a DSD surface evolution law is obtained from the rate stick front-shape and diameter-effect data. Second, the CYLEX wall motion data is used to calibrate the VAJWL energy release model via iterative hydrodynamic simulations. This process produces a JWL products EOS for the explosive. These two steps fully define the PB model. Parameterizing the RB model requires three additional steps. The Davis product EOS is constrained to the VAJWL EOS via the isentrope and CJ state, defining the RB model product state. The Davis reactants EOS is separately fit to previously available shock Hugoniot data [9] in U_s–u_p (shock speed/particle velocity) space, defining the reactant state for the RB model. The WSD reaction rate is then determined via iterative hydrodynamic simulations to match both the previously available shock initiation data and to the newly reported rate stick data. Each step is presented in detail below.

3.1. Programmed Burn Model Calibrations

3.1.1. DSD Calibration

The DSD propagation law relates the normal detonation velocity D_n to its local surface curvature κ, and is typically calibrated via the rate stick tests for steady-state detonation propagation. The model calibration process is described in detail in [30], only the essential elements are described below. Here, the functional form that represents this DSD law has a rational polynomial dependence on curvature,

$$D_n(\kappa) = D_{CJ}\left(1 - B\kappa\frac{1 + C_2\kappa + C_3\kappa^2}{1 + C_4\kappa + C_5\kappa^2}\right) \tag{2}$$

where D_{CJ}, B and C_i for $i = 2, \ldots 5$ are the propagation law parameters. With a defined set of these parameters, a set of ordinary differential equations define the DSD steady-state front shape and velocity. Previous studies [17, 30] specifically detail how this information is calculated from a given $D_n(\kappa)$ law. In addition to the DSD propagation law, the edge angle boundary condition parameter, ϕ_e, is also needed to calculate steady-state velocities and front shapes. This parameter sets the wave shape at boundaries between HE and surrounding materials and can then be used to model the influence of different confiners such as metals or plastics on wave speed and propagation speed on the HE detonation. Specifically, in the calibration of "unconfined" rate sticks, ϕ_e is taken to be the "sonic" value ϕ_s,

corresponding to the case where the detonation feels no specific confinement influence from the weak surrounding material (air), and thus the propagation speed achieves a minimum value for a given charge size.

D_{CJ} (mm/μs)	B (mm)	C_2 (mm)	C_3 (mm^2)	C_4 (mm)	C_5 (mm^2)	ϕ_s (deg.)
7.981	0.871	6.252	2.940	52.423	163.505	30.0

Table 2: Optimized DSD propagation law parameters.

The DSD parameters for PBX 9701 were obtained through minimization of a merit function incorporating the differences in phase velocity and front shapes between DSD calculations and data,

$$\mathcal{M} = \frac{W_{DE}}{N_{DE}} \sum_{i=1}^{N_{DE}} \left[\frac{(D_{0,i}^{DSD} - D_{0,i}^{exp})}{D_{0,i}^{exp}} \right]^2 + \frac{W_{FS}}{N_{FS}^T} \sum_{i=1}^{N_{DE}} \sum_{j}^{N_{FS,i}} \left[\frac{z_{ij}^{DSD} - z_{ij}^{exp}}{R_i^{exp}} \right]^2, \quad (3)$$

(as previously used in [30]) and where W_{DE} and W_{FS} balance the contribution to the overall error metric of each type of error (diameter effect vs. front shape), $D_{0,i}^{exp}$ is the i-th experimentally measured velocity, $D_{0,i}^{DSD}$ is the corresponding DSD calculation of the phase velocity, z_{ij}^{exp} is an enumeration of the experimental measurements of the front shape heights at the j-th radial coordinate within the i-th experimental data set, z_{ij}^{DSD} is the corresponding DSD calculation of the front coordinate, R_i^{exp} is the experimental charge-radius, N_{DE} is the number of diameter effect points, $N_{FS,i}$ is the number of front shape points for each case, and N_{FS} is the total number of front shape coordinates for all front shapes. For $W_{FS} = 0.25$ and $W_{DE} = 1.0$, the numerical minimization (using [33]) of this error function produces the parameters in Table 2 and the comparison of DSD calculations to data seen in Fig. 10. The relative weight factors W_{DE} and W_{FS} produced a good balance between the two types of errors. The fit represents the phase velocity and front shape data well, at a root-mean-square (RMS) error level of 6.8 m/s and 13.6 μm, respectively. Given that the repeated experiment at 6.35 mm produced a variability of 9 m/s and that experimental standard errors suggest total uncertainty ranges of 4 – 8 m/s, this level of RMS fit error is acceptable. In terms of the correspondence to the experimentally recorded front shapes, the RMS error level is within the approximate diameter of an explosive grain (44 μm) [2]. This constitutes excellent agreement, especially as the larger fit errors are concentrated near the charge-edges where the measurement uncertainty is highest.

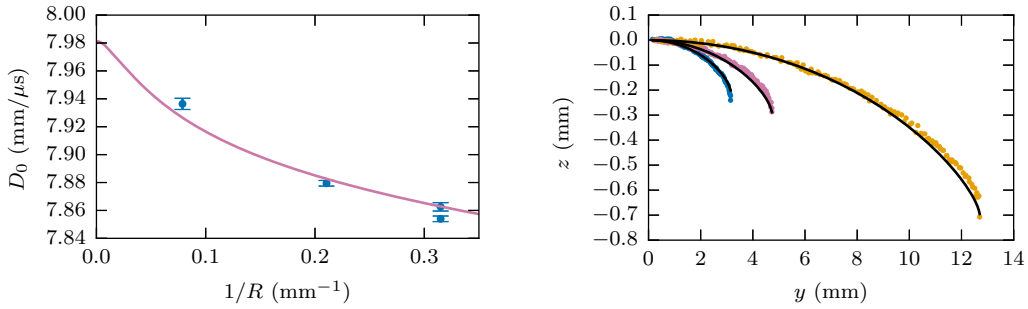

(a) (b)

Figure 10: Comparison of (a) diameter effect and (b) front shape data (symbols) to the DSD calculations (curves). The front height z is plotted against distance from the centerline y.

Figure 11 shows the PBX 9701 normal velocity dependence on curvature along with two reference explosives, PBX 9501 and PBX 9502. The results for PBX 9701 and 9502 share a turn-up in gradient near D_{CJ}, indicative of a slow reaction step being activated for large charges (or accordingly small curvature). However, the magnitude of the gradient is uniformly lower for the 9701 curve than the 9502 in the curvature range shown. In fact, the flatness of the D_n–κ curve for PBX 9701 is similar to PBX 9501 as shown. This analysis again situates PBX 9701 as a midpoint formulation for detonation performance between these two well-characterized explosives.

With the DSD law calibrated and for the purpose of simulating the CYLEX test in the PB context, detonation propagation information or timing can then be produced in a pre-processing step before the hydrodynamic phase of the calculation. The DSD calculation provides two key quantities needed in this latter phase, the time-of-arrival field of the detonation front at every point $\mathbf{x}$ in the HE geometry $t_b(\mathbf{x})$ and the local detonation front normal velocity $D_n(\mathbf{x})$ which contains the wave curvature effect imposed by the geometry and confiner on the detonation flow. To generate these quantities, a level set field ψ is typically evolved [34] according to

$$\frac{\partial \psi}{\partial t} + D_n(\kappa)|\nabla \psi| = 0, \tag{4}$$

where $\psi = 0$ represents the location of the detonation front and is evolved in time, κ is the local wave curvature (function of ψ), $D_n(\kappa)$ is defined by (2) with

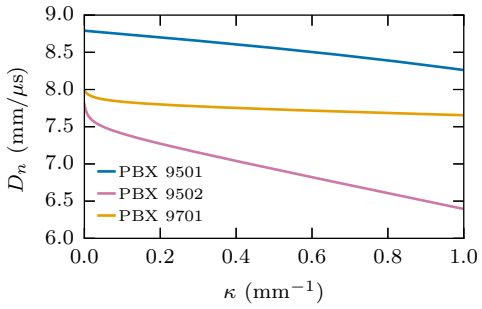

Figure 11: Comparison of the obtained $D_n(\kappa)$ function for PBX 9701 to analogues for the ideal PBX 9501 [30], and the insensitive PBX 9502.

parameters as defined in the previous section. The solution of the scalar equation in (4) also requires a boundary condition where the shape of the front at HE-confiner interfaces is set through the specification of the edge angle parameter ϕ_e (angle between shock surface normal and the confiner interface tangent vector). This value enables different strengths of confinement to affect the wave shape and velocity and can be approximately predicted from a shock polar matching analysis involving the unreacted EOS for the HE and the confiner material. Specifically for modeling of the copper and PBX 9701 interaction however, ϕ_e was determined empirically as 14.7° by fitting the available measured front shape using DSD front shape calculations and the (fixed) $D_n(\kappa)$ law developed previously, in order to maximize the fidelity of the DSD modeling of the CYLEX geometry. Figure 12 compares the result to the data. The DSD-calculated velocity using this edge angle is then 7.927 mm/μs, within a few m/s from the measured value. Note that for computational simplicity in the forthcoming CYLEX modeling using DSD, we have chosen to ignore the thin Sylgard layer that binds the HE and copper as this has a minimal effect on metal push.

3.1.2. VAJWL Product EOS Calibration

The analytical EOS form known as the Jones-Wilkins-Lee (JWL) equation of state has long been used to model the behavior of HE gaseous products [35], here

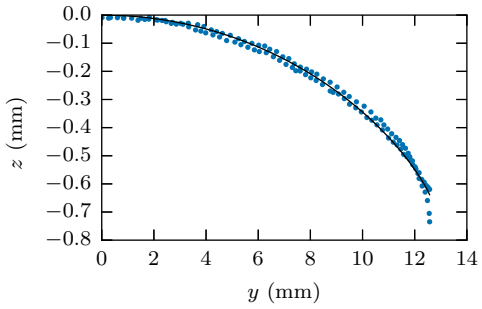

Figure 12: Comparison of the DSD calculated front shape for the CYLEX test to the experimental measurement.

it can be defined with respect to its $p = p(v, e)$ form,

$$p(v,e) = A\left(1 - \frac{\omega v_0}{R_1 v}\right)\exp\left(-\frac{R_1 v}{v_0}\right) + B\left(1 - \frac{\omega v_0}{R_2 v}\right)\exp\left(-\frac{R_2 v}{v_0}\right) + \frac{\omega}{v}(e - e'), \tag{5}$$

where v is the specific density, e is specific internal energy, e' is chosen by convention such that at ambient conditions, $p(v_0, 0) = 0$, where v_0 is the ambient specific density, and the constant JWL EOS parameters are A, B, R_2, R_1 and ω. In the context of engineering design calculations, the $p(v, e)$ relation has been augmented with an near-instantaneous energy release term that activates at a pre-programmed "burn time" to form an inexpensive detonation performance PB model,

$$p(v,e) = A\left(1 - \frac{\omega v_0}{R_1 v}\right)\exp\left(-\frac{R_1 v}{v_0}\right) + B\left(1 - \frac{\omega v_0}{R_2 v}\right)\exp\left(-\frac{R_2 v}{v_0}\right) + \frac{\omega}{v}(e - e' + \lambda E_{det}), \tag{6}$$

where $\lambda(t, \mathbf{x})$ refers to the pre-programmed reaction progress (becoming non-zero only upon the calculated time of arrival at a particular time t and location $\mathbf{x}$) and E_{det} is the detonation energy which is then released over a few computational cells. When the timing component responds to a propagation law having a constant normal speed or the Chapman-Jouguet speed (known alternatively as the "Huygens construction"), the resulting methodology is a standard programmed burn method that has long served as the basis for hydrocode-based calibration of

the products EOS. For example, Mortensen and Souers [36] use this basic PB methodology to calibrate a series of explosives to various CYLEX tests, iteratively refining the input JWL EOS parameters by minimizing the difference between experimental measurement of the wall motion and calculation. However, this standard PB method has a significant drawback: since the wave speed is defined as constant in calculating the time-of-arrival, the application of (6) results in a immediate transition to the CJ state for the processed HE material across the entire (flat) front surface in the cylinder. This is a significant simplification since HE detonation wave fronts are generally curved and this is manifested in significantly slower wave speeds and reduced shock strength (where the magnitude of the effect depends on the type of explosive). These real-world effects are therefore unaccounted for in this standard PB methodology. This provides the primary motivation for our modification of the process to determine the products EOS by incorporating wave curvature effects into the CYLEX modeling. Details of the implementation of this new development are described in the following.

The DSD timing model is often paired with an extension of the JWL product equation of state [35] to compose a PB method that responds to variations in shock strength [14, 15]. Known as the Velocity-Adjusted Jones-Wilkins-Lee (VAJWL) methodology, it functions by modulating the product state (and thus the applied rate of energy release) to be consistent with changes in DSD surface wave speed. (The wave speed is, in turn, related to the local curvature given by the DSD propagation law.) Here, we only briefly describe the VAJWL method, with additional detail provided in [14, 37]. The VAJWL method relies on hydrodynamic simulations that solve the compressible Euler equations in the post-shock HE region,

$$\begin{aligned} &\frac{\partial \rho}{\partial t} + \nabla \cdot (\rho \mathbf{u}\,) = 0, \\ &\frac{\partial}{\partial t}(\rho \mathbf{u}\,) + \mathbf{u}\,\nabla \cdot (\rho \mathbf{u}\,) + \rho(\mathbf{u} \cdot \nabla)\mathbf{u} + \nabla p = 0, \\ &\frac{\partial}{\partial t}(\rho E) + \nabla \cdot (\mathbf{u}\,(\rho E + p)) = 0, \end{aligned} \tag{7}$$

where ρ, $\mathbf{u}$, E and p are the density, material velocity vector, specific total energy and pressure, respectively. The HE total energy depends on the specific internal energy e and local particle velocity vector $E = e + \frac{1}{2}(\mathbf{u} \cdot \mathbf{u})$. The $p = p(v, e)$

relation for solution of (7) is a modification of (6),

$$p(v,e) = \tilde{A}(D_n)\left(1 - \frac{\omega v_0}{\tilde{R}_1(D_n)v}\right)\exp\left(-\frac{\tilde{R}_1(D_n)v}{v_0}\right) + B\left(1 - \frac{\omega v_0}{R_2 v}\right)\exp\left(-\frac{R_2 v}{v_0}\right) + \frac{\omega}{v}(e - e' + \lambda E_{det}), \tag{8}$$

where λ is now determined by the DSD-calculated time of arrival rather than the constant speed of propagation of the simpler Huygens model. An additional, crucial difference with (6) involves the equation of state parameters, i.e. $\tilde{A}$ and $\tilde{R}_1$ are perturbed or "velocity-adjusted" JWL parameters that depend on the localized D_n encountered by a particular fluid particle at an initial location $\mathbf{x}$. This is achieved by requiring that $\tilde{A}$ and $\tilde{R}_1$ generate a lower Chapman-Jouguet (CJ) velocity for each fluid element that is equal to the local D_n (without modifying E_{det} and constrained to the input EOS parameters, i.e. A, B, R_1, R_2 and ω). This modifies the expansion profile for consistency with the reduced DSD surface wave speed, while keeping the lower pressure regime of the equation of state largely unaffected. Note that if $D_n = D_{CJ}$, we recover the classic PB method defined in (6) such that $\tilde{A} = A$ and $\tilde{R}_1 = R_1$ where A and R_1 are the input or non-velocity adjusted products EOS parameters. This approach differs with that of Hetherington and Whitworth [14], who instead velocity-adjust $\tilde{A}$ and $\tilde{B}$ to achieve a similar result where this latter approach modifies a wider range of the EOS behavior.

The calibration of the VAJWL model is coupled to material models for the copper outer confinement whose motion is obtained from experiment. The confining copper material was modeled using a tabular equation-of-state detailed in Peterson et al. [38] and its plastic deformation under shock loading from the HE was modeled according to Preston et al. [39]. Figure 13 shows the HE pressure field and the inner wall boundary location of the copper tube for a VAJWL CYLEX simulation. This snapshot is taken well after the wave has attained a steady state propagation. This latter fact is proven in Fig. 14 through a comparison of the simulated wall velocity profiles at various axial stations. These profiles (shifted to the wave arrival time for each axial measurement location) all converge or overlay once the wave has exceeded an axial distance of 2-4 charge-diameters from the initiation face of the explosive. This justifies our subsequent comparisons of the simulated wall motion and the experimental counterparts.

A large number of successive CYLEX simulations are needed to refine the unperturbed EOS for the products, which will be obtained from numerically minimizing differences between calculation and experiment. The relevant simulations

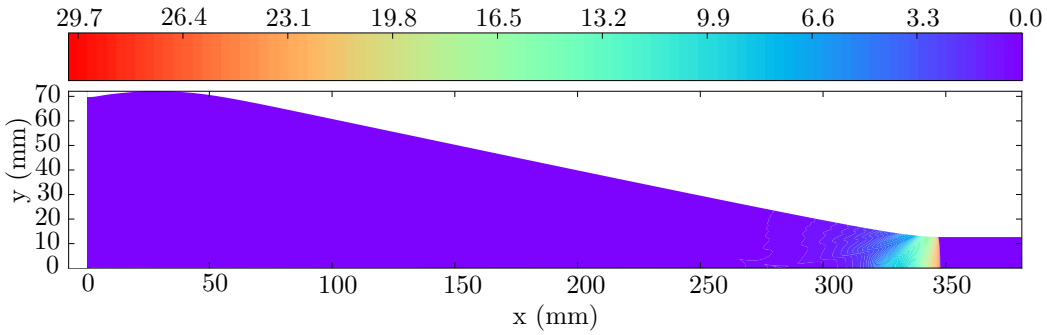

Figure 13: A snapshot of the pressure profile in the HE region of a CYLEX simulation near the end of the simulation.

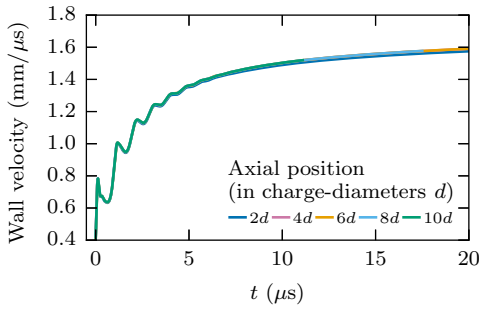

Figure 14: Comparison of simulated PDV traces (shifted to the post-shock arrival time) for the VAJWL detonation performance model at various axial stations (relative to charge-diameter d).

were performed in the multiphysics, multimaterial Lagrangian hydrodynamics code FLAG [40, 41] to enable the use of the cited material models in the HE and copper confiner. The FLAG "hydrocode" uses spatially staggered, unstructured polyhedral grids with a finite-volume spatial discretization and explicit time integration of the conservation laws in (7) and an artificial-viscosity-based shock treatment. For any given set of EOS parameters, the hydrocode simulations are used to generate the corresponding wall motion profiles at the outer copper surface when the detonation is propagating steadily. The numerically minimized error merit function used to produce the optimal EOS parameters was simply the averaged sum of the root-mean-square errors for the 4 measurements of the wall velocity ($\mathbf{v}_{expt}^{probe}$) with respect to the calculated post-shock wall motion velocity

($\mathbf{v}_{calc}$),

$$\mathcal{M} = \frac{1}{4} \sum_{probe=1}^{4} RMS(\mathbf{v}_{data}^{probe} - \mathbf{v}_{calc}) \tag{9}$$

where $RMS(\mathbf{x}) = \sqrt{\sum_i^N \mathbf{x}_i^2 / N}$ where N is the number of elements in a given vector $\mathbf{x}$. The numerical algorithm chosen to numerically minimize this merit function was a downhill simplex method [33].

The initial set of the EOS parameters in Eq. (8) were generated according to a recent correlation developed by Jackson [22] finding that detonation product EOS quantities scale with the reactant kinetic energy ($\rho_0 D_0^2$) where ρ_0 is the initial HE density and D_0 is the measured detonation phase velocity. After a sensitivity study, it was found that it was sufficient to modify only two input EOS parameters, A and B, during the optimization to obtain sufficient quality fits (retaining B, R_2 and ω from the initial definition). Note that this methodology was also recently used to accelerate the equivalent calibration process for the ideal explosive LX-19 [37]. Additionally, at every iteration in the optimization process, a constraint was

A (GPa)	B (GPa)	R_1	R_2	ω	E_{det} (kJ/g)	ρ_0 (g/cm^3)
624.077	12.213	4.534	1.369	0.3043	5.205	1.692

Table 3: Final calibrated VAJWL model EOS parameters. Note that only A and B were optimized and at each iteration E_{det} was set such that the CJ velocity was consistent with the $D_n(\kappa)$ relation counterpart. The remaining parameters were not modified from the initial definition provided by the method of Jackson [22]. The CJ state velocity, pressure and specific volume were 7.9816 mm/μs, 27.9730 GPa and 0.4376 cm^3/g, respectively.

applied to the detonation energy parameter E_{det} to ensure the input JWL CJ speed was equal to the D_{CJ} parameter in the $D_n(\kappa)$ relation, namely 7.981 mm/μs. Finally, after a convergence study for the wall motion profile, a resolution of 250 μm was selected to calibrate the EOS, balancing computational speed while retaining the ability to represent the ringing feature in the wall motion. The resulting calibrated products EOS parameters appear in Table 3 and indicate that PBX 9701 has an TNT energy equivalence of 1.24.

The wall motion calculation derived from the optimized VAJWL model appears in Fig. 15 (along with several relevant reference calculations as well).

The correspondence to experiment for the calibrated model is good, lying mostly

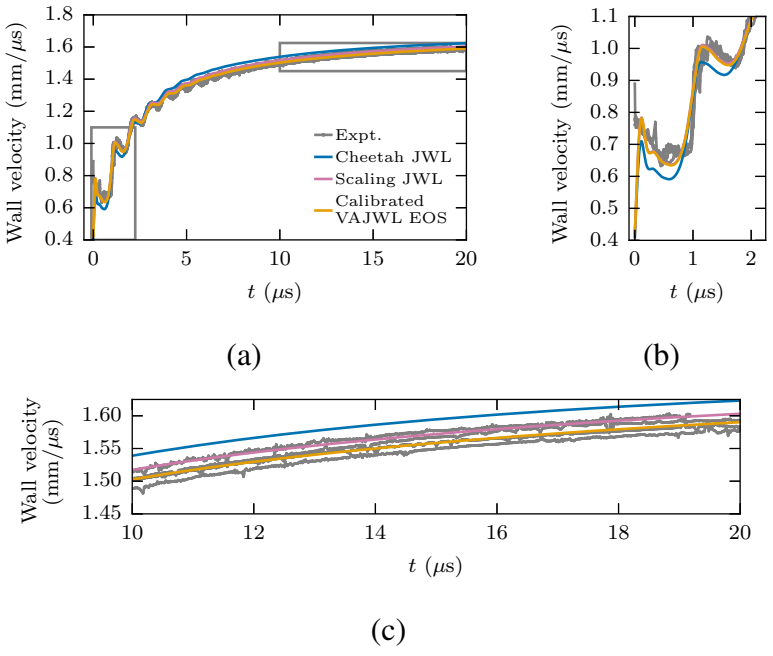

Figure 15: (a) CYLEX wall motion comparison between calibrated VAJWL model and data. Inset in shows zoomed regions or detail at (b) early and (c) late time (as indicated by the outlines in (a)). The traces are plotted as functions of time (t) from the wave arrival at each probe's axial location on the copper tube's surface. Both experimental and simulated traces are placed at axial locations that ensure steady-state propagation of the wave (i.e. at least 4 charge-diameters from the initiating surface) and therefore the specific location or identity of the probe is immaterial in these comparisons.

within the experimental variability as determined from the variations in wall motion recorded by each of the four probes. For reference, Fig. 15 also includes results from two additional VAJWL models composed of the current PBX 9701 DSD relation and two products JWL EOSs: the initial products EOS definition derived from scaling model in Jackson [22] and a thermochemical calculation (using Cheetah v.7 with the *exp6.v7.1.chl* product database [42]). Figures 15b-c show early and late time zoomed regions of the motion to highlight differences between calculations and data. The Cheetah prediction is interesting in that it is both under- and over-energetic at different points in the wall motion evolution. It

should also be mentioned that the scaling model is close to the data, providing an excellent starting point for the iteration process. The isentropes for each of these component JWLs and the calibrated counterpart are shown in Fig. 16. In addition, the inset in this figure shows how the reference JWLs relate to the calibrated result (by evaluating the functional difference in the shown range). These differences largely explain why the Cheetah result is underpowered at higher pressures relative to the VAJWL-derived result but then overtakes it at lower pressures (as reflected in the wall motion motion). Additionally, the scaling model is shown to be close to the calibrated EOS result but does differ especially at higher pressures.

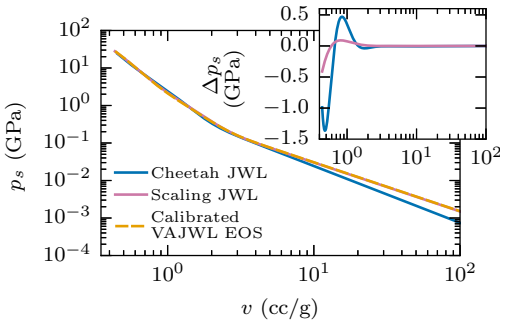

Figure 16: Comparison of JWL pressure isentropes for PBX 9701 on a log-log scale. The inset gives the difference (Δp_s) between the reference JWLs and the calibrated JWL on the shown range in v.

3.2. Reactive Burn Model Calibrations

Reactive burn models require equations of state for the products, the unreacted explosive, a thermodynamic closure between the two phases and a reaction rate model, setting the conversion between the phases. The EOSs for products and reactants are distinct phases, defined and calibrated separately. We use the empirical EOSs originally developed by Davis et al [13, 43], as presented in Wescott et al. [6], which have been shown to readily fit calibration experiments for a variety of plastic bonded explosives [6, 44]. These equations are presented in Appendix A. How each of these model elements are obtained or defined is described below.

3.2.1. Reactant EOS Calibration

Each instance of the Davis reactant EOS is fully defined by Equations A.1–A.6 with parameters A, B, C, Γ_R^0 and Z. All of these model parameters were

calibrated (except Z) to the experimental reactant EOS data that appears in [9] for an explosive with a reported 95% DAAF and 5% Kel-F 800 formulation in the absence of published data for PBX 9701. Note that while this formulation shares both of its components with PBX 9701, there is a 2% difference in DAAF content. The calibration methodology uses a similar approach to [45]. The result for the Hugoniot appears in Fig. 17 and specific parameters in Table 4.

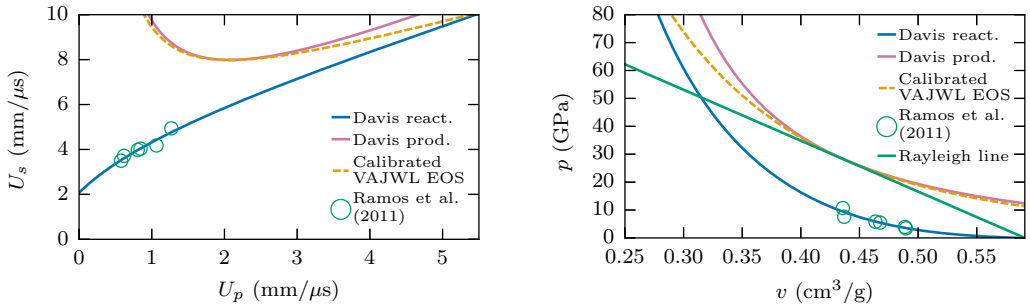

(a) (b)

Figure 17: Reactants and products EOS Hugoniot data and results from model fits in both $p - v$ and $U_s - U_p$ planes. The PBX 9701 JWL was derived from the previous VAJWL EOS calibration.

A (mm/μs)	B	C	Γ_R^0	Z	ρ_0 (g/cm^3)	T_0 (K)
2.0753	3.0728	0.3519	0.6988	0.0	1.692	293.0

Table 4: Calibrated Davis reactants EOS parameters to $U_s - U_p$ data from Ramos et al [9].

3.2.2. Product EOS Calibration

The Davis product EOS is defined by Equations A.7–A.12 with parameters p_c, v_c, a, k, n, and b. The reference internal energy E_{det} sets the energy released by reaction completion. The Davis form in this case was fitted directly to the isentrope determined from the previous analysis of the products EOS for the VAJWL model. A merit function approach was adopted for this purpose, employing the

JWL EOS isentrope and CJ state ($p_s^{JWL}, p_C J^{JWL}, D_{CJ}^{JWL}, v_{CJ}^{JWL}$) as reference data for the varied Davis products equivalents ($p_s^{Davis}, p_C J^{Davis}, D_{CJ}^{Davis}, v_{CJ}^{Davis}$), i.e.

$$\begin{aligned}\mathcal{M}_{EOS} = \beta_1 \sum_i^N (p_s^{Davis}(v_i) - p_s^{JWL}(v_i))^2/N + \\ \beta_2(p_{CJ}^{Davis} - p_{CJ}^{JWL})^2 + \beta_3(D_{CJ}^{Davis} - D_{CJ}^{JWL})^2 + \beta_4(v_{CJ}^{Davis} - v_{CJ}^{JWL})^2,\end{aligned} \tag{10}$$

where β_i are weight constants that can promote the reduction of a specific error component, v_i represents the N specific volume values enumerated by i at which the isentropes were functionally compared. Specifically, the weight constants were chosen such that a good balance between the different types of errors was obtained, i.e.

$$\beta_1 = 1.0,\ \beta_2 = 0.25,\ \beta_3 = 1.0,\ \beta_4 = 0.1, \tag{11}$$

and additionally, v_i represents $N = 500$ evenly distributed points between v_{CJ}^{JWL} and 7.0 cm^3/g. Clearly, this merit function definition is not unique and a set of different choices will produce a range of results. For this reason, the wall motion response that results from this calibration is evaluated in section 3.2.6 to ensure its accuracy. The EOS parameters a, p_c, v_c and n were used to numerically minimize this function (using the Nelder-Mead algorithm [33]), while E_{det}, k and b were held fixed. The Hugoniot that is produced from this process appears in Fig. 17. A comparison between the JWL isentrope and the Davis form appears in Fig. 18. The inset in Fig. 18 shows the difference in the isentropes, showing in particular that the Davis model is slightly higher near CJ conditions than the JWL, then dips below (denoted by red region of the curve) and finally settles into a small positive difference of < 0.01 GPa. The maximum difference in the included range is about 0.4 GPa. These differences are manifested later on when comparing the CYLEX test wall motion derived from performance calculations. The parameters of the product EOS appear in Table 5.

3.2.3. Closure

In the reaction zone where reactants and products coexist, the HE state assumes a dual definition which requires a closure relation relating the thermodynamic state of a fluid element's two phases. In the original definition of the WSD reactive burn model [6], the $p - T$ closure is preferred. Here, we utilize the $p - \rho$ closure instead which introduces substantial computational advantages in terms

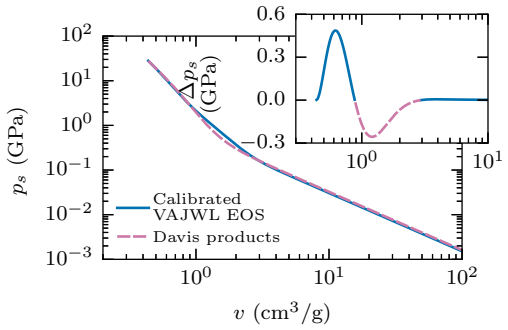

Figure 18: Comparison of isentropes between JWL and David products form. Inset shows differences between the two isentropes on a linear vertical scale and log horizontal scale where the solid and dashed line segments denote regions where the Davis EOS is above and below the JWL parameterization obtained in the PB calibration process, respectively.

a	b	n	k	v_c (cm^3/g)	p_c (GPa)	ρ_0 (g/cm^3)	E_{det} (kJ/g)
0.6999	0.5800	2.0880	1.3043	0.8381	3.8241	1.692	5.205

Table 5: Calibrated Davis products to the JWL products equation determined via the VAJWL calibration process. The CJ velocity for the Davis form was 7.982 mm/μs and the pressure was 27.97 GPa (both constrained to the calibrated JWL as well).

of efficiency and robustness due to the closed form solution for the dependence of the mixture p on e and v, i.e.

$$p = p_R = p_P, \; v = v_R = v_P, \tag{12}$$

with the specific internal energy taken as a mass-weighted sum of the reactant and product internal energies,

$$e = (1 - \lambda)e_R + \lambda e_P, \tag{13}$$

where the subscripts R and P refer to the reactant and product state, respectively. This closure has been used successfully by Desbiens et al. [46], Matignon et al. [47] to represent initiation and propagation data in their HE calibrations. This closure choice in conjunction with the WSD model [6] has also been used in the

HE model calibration of PBX 9501 and 9502 [48, 49] and additionally, both of these studies included model validation in circular arc geometries.

3.2.4. WSD Reaction Rate Calibration

The WSD reaction rate is defined by Equations A.13–A.20. The various rate terms depend on the local pressure (p), density (ρ), shock density (ρ_s) and reaction progress (λ) and on a number of rate parameters, categorized by the regime in which they primarily affect the reaction rate: for initiation and ignition (r_I and r_{IG}), k_I, b, a_I, n_I, k_{IG}, n_{IG}, ρ_c and for detonation propagation (r_{DG}), k_{DG}, c, d, n_{DG}, e, n_B,λ_S and k_B. The fact that the various parameters can be split into distinct regimes (with unique calibration experiments for each) allows for the sequential calibration of the parameters [6]. Note, however, that there are shared parameters between the r_{IG} and r_{DG} rates, namely c and d and these two terms are blended via W during initiation as determined by the parameter ρ_c. So, in effect, although the propagation rate terms r_{DG} and r_B are independent of the remaining initiation parameters for $\rho_s > \rho_c$, the converse is not necessarily true. Therefore, firstly, we choose to calibrate the propagation phase and then subsequently adjust the initiation parameters to arrive at the final reaction rate model.

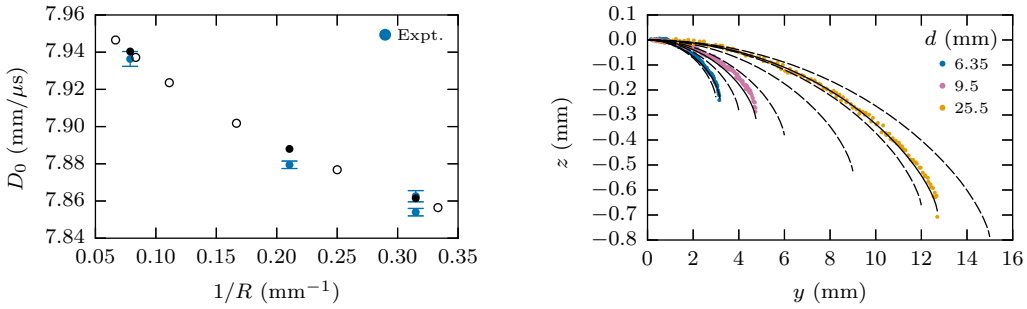

(a) (b)

Figure 19: Calculations from calibrated model (in black symbols/lines) compared against the source (a) diameter effect and (b) front shape data. In (a), the filled black circles denote the charge-sizes simulated in the calibration process, open black circles correspond to uncalibrated charge-sizes. In (b), the dashed curves denote uncalibrated charge-size data while solid black lines indicate front shapes included in calibration. The employed resolution is equivalent to about 4 points in the fast reaction layer and 132 over the entire span of the RZ.

Propagation rate terms. The calibration of the propagation rate term parameters is through the unconfined rate stick tests, which provide a measure of the effect of flow divergence on the steady-state multi-dimensional reaction zone. The shock-attached computational technique we use to determine the phase velocities and front shapes for comparison to the recorded unconfined data is described in [16, 48, 49]. The same experimental measurements are used in the merit function minimization for the rate parameters, equivalently to the DSD calibration detailed previously. Therefore, the merit function is as in (3), where the computational data is now the steady-state data obtained via the RB rate stick simulations. Again, one of our goals in this work has been to generate consistent detonation propagation information between the PB methodology and its RB counterpart. Therefore, we have striven to use the exact same procedure for determining the model's timing component. The numerical algorithm to achieve this is also similar to the DSD case [33] and a resolution of 10 μm was used during the optimization process (equivalent to 2 points in the fast reaction layer and about 66 in the slow reaction layer). This resolution was chosen as it provides computational efficiency (hundreds of rate stick simulations are needed) while also giving reasonably converged steady-state calculations relative to the experimental error and variability. This fact is confirmed by using finer resolutions with the model obtained at the coarser (calibration) resolution. In particular, the results in Fig. 19 use a base resolution of 5 μm and retain a good comparison to the data (comparable to the DSD case). The optimized parameter set appears in Table 6.

k_{DG} ($1/\mu$s GPa$^{n_{DG}}$)	c	d	n_{DG}	e	n_B	λ_S	k_B ($1/\mu$s GPa^{n_B})
0.0205	0.3478	0.2432	2.8269	0.5	0.4159	0.9	0.0410

Table 6: The calibrated reaction rate parameters for the detonation propagation phase.

Initiation terms. The remaining parameters which deal with the initiation and ignition of the detonation wave were calibrated separately and in reference to Pop-plot data obtained by Ramos et al [9]. The calibration of these terms therefore require the simulation of plate impact experiments where the HE initiation takes place via a planar shock, with varying strengths to produce different run-to-detonation distances. The one-dimensional simulations of the gas-gun experiments took place in the previously described FLAG hydrocode. Each calculation uses the different input pressures to shock the HE material and we calculate the

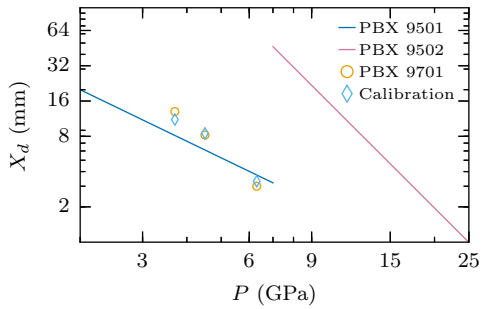

Figure 20: The available PBX 9701 Pop-plot data [9]. The calculations used a finest level resolution of 2.5 μm (leading to converged results in run-distance). For reference, empirical curve fits to Pop-plot data for PBX 9501 [50] and 9502 [51] also appear, again situating PBX 9701 as intermediate in terms of the shock-to-detonation transition.

run distance to detonation, as judged by intersecting linear shock track fits to the early and late time calculated shock track data. As in the other model components, the optimized ignition growth rate parameters (a, r_{IG}, ρ_c and n_{IG}) were obtained from minimization of an error function, i.e.

$$\mathcal{M} = \sum_{i=1,2,3} [X_{d,i}^{calc} - X_{d,i}^{exp}]^2, \tag{14}$$

where $X_{d,i}^{exp}$ is the experimental run distance and $X_{d,i}^{calc}$ is the corresponding calculated run distance. We again used the downhill simplex methodology to achieve this [33]. The calibration simulations used 5 μm to iterate on the parameters. The optimal parameter set that results appears in Table 7 and the relevant calculations are also plotted in Fig. 20 (employing a finer resolution of 2.5 μm to confirm the convergence of the run-distances calculated in the calibration process). Note that k_I, b, and x were not optimized as they were not necessary to generate the generally good correspondence to the data (they take provisional values from previous 9502 modeling [6]). It should be highlighted that the initiation data is well-represented using the $p - \rho$ closure, a fact that had been demonstrated for the WSD rate in the detonation propagation regime [48, 49] but now extended to the initiation regime. Figure 20 also presents trend lines for PBX 9501 and 9502 for reference (via experimentally derived empirical curve fits). Comparison to these other explosives confirms that PBX 9701 is mostly intermediate in shock sensitivity (though much closer to HMX-based 9501) as judged via the input pressure

k_I (μs^{-1})	x	b	a	k_{IG} (μs^{-1} GPa$^{-n_{IG}}$)	n_{IG}	ρ_c (g/cm^3)
1e+05	7.0000	0.6667	0.1561	0.0512	1.3508	2.2314

Table 7: The reaction rate parameters for the initiation phase (a, k_{IG}, n_{IG} and ρ_c were optimized).

and run distance metrics.

3.2.5. ZND profile

For the Zeldovich-von Neumann-Döring (ZND) wave, the model that is produced in this process has two main scales during detonation propagation, the fast scale (on the order of 10 μm) and the much longer slow scale of around 663 μm (c.f. Fig. 21). This is indicative of an insensitive explosive although it should be noted that the fast scale is much finer than a similar scale for PBX 9502 [48] and comparable to the conventional HE PBX 9501 as shown in Fig. 21. This feature is associated with the relatively low gradient of the diameter effect data for PBX 9701 relative to PBX 9502, necessitating a faster reaction to accommodate this (see diameter effect curve comparison for these explosives in Fig. 6b). Furthermore, this also implies that detonation wave failure for PBX 9701 also occurs at a significantly reduced charge-size, again in comparison to PBX 9502.

3.2.6. CYLEX reactive burn simulation

The completed reactive flow model is now used to simulate the CYLEX test in the FLAG hydrocode to compare to the experimental copper wall acceleration and confirm the consistency of the RB products EOS with its source and counterpart derived in the PB calibration process. The results of this study appear in Fig. 22 (for various resolutions for the RB model). We note that the experimental wall motion is well represented even at a coarse resolution (relative to the ZND fast reaction zone length scale), again confirming that most of the work occurs in the post-RZ region and that the physical time and length scales in this region increase relative to the much finer RZ counterparts. However, we caution that although the wall motion is accurately represented, the RZ profiles and therefore the calculated phase velocities are still experiencing significant changes at these resolutions. This observation provides some evidence that CYLEX wall motion measurements *alone* are not an effective validation of the RB model reaction zone structure as the predicted wall motion mainly depends on the product EOS parameterization.

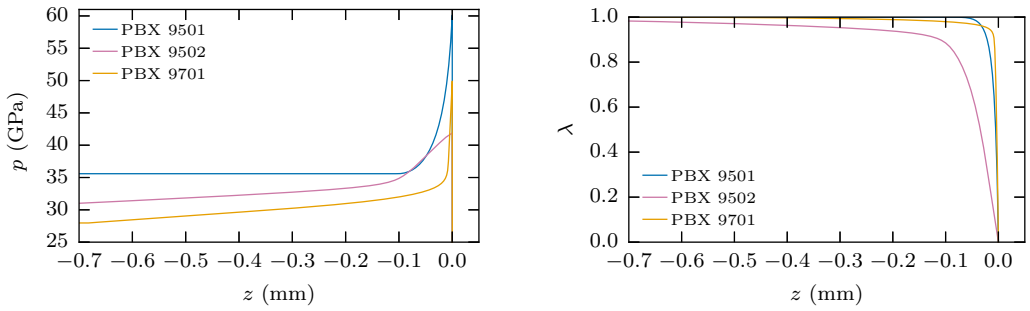

(a) (b)

Figure 21: The one-dimensional steady-state CJ wave structure as function of distance from the shock (z) for (a) p and (b) λ for the PBX 9701 model. The fast reaction length scale is about 10 μm while the total reaction zone scale is around 663 μm. For reference, equivalent calculations are included for PBX 9501 [49] and 9502 [48] models.

Figure 22b-c show zoomed regions to highlight early and late time evolution and the differences between calculations and data. In particular, the initial jump is well-captured by the RB results but there is a slight overshoot on the second ring in the RB model relative to the data. The late time inset shows that the RB results are on the lower side of the experimental variability (as represented by the multiple probe results). Also included in Fig. 22a-b is the calibrated VAJWL model result which also shows some deviations with respect to the RB results which are ascribed to dissimilarities in the PB/RB methodologies and additionally, the slight differences in terms of the isentrope functional behavior (see Fig. 18).

4. Conclusions

Detonation performance experiments and model calibrations have been performed for the reduced-sensitivity explosive PBX 9701, composed of 97% DAAF explosive and 3% Kel-F 800 binder by weight. Detonation performance measurements presented included front-curvature rate sticks at multiple diameters and cylinder expansion (CYLEX) test data, while prior shock initiation data was also reviewed. These data were used to calibrate both a programmed burn (PB) and reactive burn (RB) model to enable both an evaluation of the PBX 9701 detonation performance characteristics relative to conventional and insensitive explosives, and to provide a new capability for engineering calculations with PBX

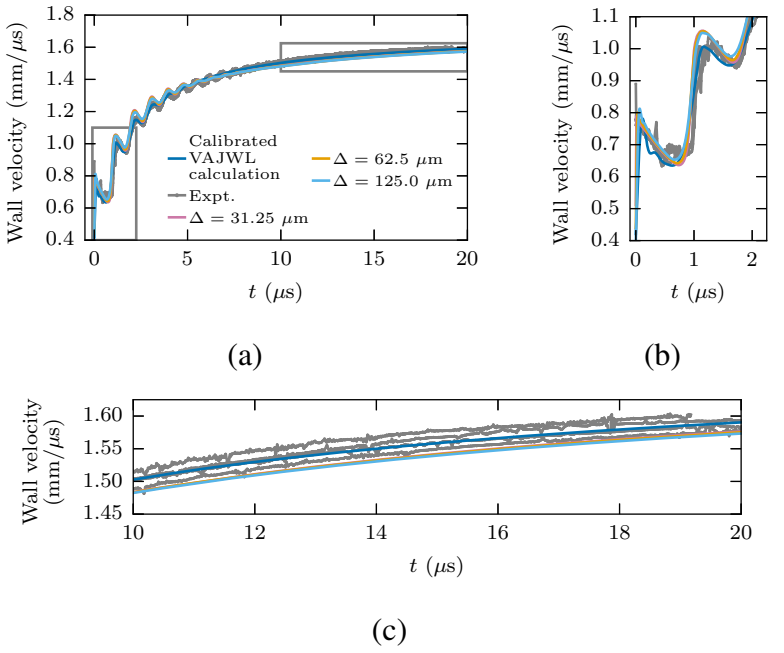

Figure 22: Calculated wall motion for the RB model for various resolutions (Δ) for (a) entire span in time and two zoomed regions at (b) jump off and (c) late time in the wall evolution. The experimental data and VAJWL model results are also plotted for reference.

9701. The PB model consisted of a Detonation Shock Dynamics (DSD) timing component with a Velocity-Adjusted Jones-Wilkins-Lee Product (VAJWL) energy release component. The reactive burn model was the Wescott-Stewart-Davis (WSD) model using the $p - \rho$ closure. Overall, PBX 9701 is seen to exhibit improved performance relative to insensitive explosives like PBX 9502, with a TNT equivalence of 1.24 and performance properties that are well captured by existing models.

A new development in the calibration process linked the product equation of state (EOS) response in the RB model to the PB counterpart to create a consistent Chapman-Jouguet (CJ) state, isentrope behavior and corresponding wall motion profile between the models. In addition, the detonation propagation aspect of each model has been calibrated consistently via the minimization of a common error metric. This should facilitate the comparison of the two modeling methodologies. This is in contrast to the usual RB model calibration methodology which aims to

avoid the direct simulation of the CYLEX test, and so the products EOS is either populated with thermochemical equilibrium calculations such as those extracted from Cheetah [42] (which are of limited accuracy) or an analytical reduction of the wall motion profile [21] (which tends to limit its validity to lower non-CJ pressures). In particular for PBX 9701, the Cheetah result considerably underpredicts D_{CJ} and p_{CJ} (i.e. 7.809 mm/μs and 24.14 GPa, respectively) versus 7.981 mm/μs and 27.97 GPa determined from our analysis of the experimental data set, a difference of nearly 200 m/s and 4 GPa, respectively. This discrepancy is most likely tied to shortcomings in the physical assumptions of the thermochemical equilibrium approach itself, i.e. the approximate fluid mixing rules of the product species or the lack of a true chemical equilibrium in real detonation flows, especially for explosives that exhibit fast and slow reaction structure like PBX 9502 or PBX 9701. Nevertheless, the Cheetah result functions as a useful reference point to dimension the accuracy of the current hydrocode-based calibration results.

Acknowledgments

The authors are grateful to Stephanie Hagelberg and Sam Vincent for assistance with the experimental preparation and test execution.

References

[1] E. G. Francois, D. E. Chavez, M. M. Sandstrom, The development of a new synthesis process for 3,3'-diamino-4,4'-azoxyfurazan (DAAF), Prop. Expl. Pyro. 35 (6) (2010) 529–534.

[2] E.-C. Koch, Insensitive high explosives II: 3, 3-Diamino-4, 4-azoxyfurazan (DAAF), Prop. Expl. Pyro. 41 (3) (2016) 526–538.

[3] J. B. Bdzil, D. S. Stewart, Modeling two-dimensional detonations with detonation shock dynamics, Phys. Fluids A: Fluid Dyn. 1 (1989) 1261.

[4] J. B. Bdzil, D. S. Stewart, The dynamics of detonation in explosive systems, Annu. Rev. Fluid Mech. 39 (2007) 263–292.

[5] J. B. Bdzil, W. Fickett, D. S. Stewart, Detonation shock dynamics: a new approach to modeling multi-dimensional detonation waves, in: Proceedings of the 9th International Detonation Symposium, Office of Naval Research, 730–42, 1989.

[6] B. L. Wescott, D. S. Stewart, W. C. Davis, Equation of state and reaction rate for condensed-phase explosives, J. Appl. Phys. 98 (2005) 053514.

[7] B. C. Tappan, P. R. Bowden, J. P. Lichthardt, M. M. Schmitt, L. G. Hill, Evaluation of the detonation performance of insensitive explosive formulations based on 3, 3' Diamino-4, 4'-Azoxy furazan (DAAF) and 3-Nitro-1, 2, 4-Triazol-5-One (NTO), J. Ener. Mat. 36 (2) (2018) 169–178.

[8] D. Chavez, L. G. Hill, M. Hiskey, S. Kinkead, Preparation and explosive properties of azo- and azoxy-furazans, J. Ener. Mats. 18 (2-3) (2000) 219–236.

[9] K. Ramos, J. Morris, E. Francois, Unreacted Hugoniot and shock initiation measurements in Diaminioazoxyfurazan (DAAF), Tech. Rep. LA-UR-11-03774, Los Alamos National Laboratory, Los Alamos, NM, USA, 2011.

[10] E. L. Lee, C. M. Tarver, Phenomenological model of shock initiation in heterogeneous explosives, Phys. Fluids 23 (12) (1980) 2362–2372.

[11] E. L. Lee, H. C. Horning, J. W. Kury, Adiabatic expansion of high explosives detonation products, Tech. Rep. UCRL 50422, Lawrence Livermore National Laboratory, Livermore, CA, USA, 1968.

[12] E. L. Lee, M. Finger, W. Collins, JWL equation of state coefficients for high explosives, Tech. Rep. UCID-16189, Lawrence Livermore National Laboratory, Livermore, CA, USA, 1973.

[13] W. C. Davis, Complete equation of state for unreacted solid explosive, Combust. Flame 120 (3) (2000) 399–403.

[14] D. C. Hetherington, N. J. Whitworth, A simple model for the dependence on local detonation speed of the product entropy, in: AIP Conference Proceedings, vol. 1426, AIP, 259–262, 2012.

[15] A. N. Hodgson, C. A. Handley, DSD/WBL-consistent JWL equations of state for EDC35, in: AIP Conference Proceedings, vol. 1426, AIP, 247–250, 2012.

[16] C. Chiquete, M. Short, C. D. Meyer, J. J. Quirk, Calibration of the Pseudo-Reaction-Zone model for detonation wave propagation, Combust. Theory Modell. (2018) 744–776.

[17] S. I. Jackson, M. Short, Scaling of detonation velocity in cylinder and slab geometries for ideal, insensitive and non-ideal explosives, J. Fluid Mech. 773 (2015) 224–266.

[18] J. B. Bdzil, Steady-state two-dimensional detonation, J. Fluid Mech. 108 (1981) 195–226.

[19] C. A. Handley, B. D. Lambourn, N. J. Whitworth, H. R. James, W. J. Belfield, Understanding the shock and detonation response of high explosives at the continuum and meso scales, Appl. Phys. Rev. 5 (1) (2018) 011303.

[20] G. I. Taylor, Analysis of the explosion of a long cylindrical bomb detonated at one end, Mechanics of Fluids, Scientific Papers of GI Taylor 2 (1941) 277–286.

[21] S. I. Jackson, An analytic method for two-dimensional wall motion and product isentrope from the detonation cylinder test, Proc. Combust. Inst. 35 (2) (2015) 1997–2004.

[22] S. I. Jackson, Scaling of the detonation product state with reactant kinetic energy, Combust. Flame 190 (2018) 240–251.

[23] S. I. Jackson, Scaled cylinder test experiments with insensitive PBX 9502 explosive, in: Proceedings of the 15th International Detonation Symposium, Office of Naval Research, 171–180, 2015.

[24] S. I. Jackson, The dependence of Ammonium-Nitrate Fuel-Oil (ANFO) detonation on confinement, Proc. Combust. Inst. 36 (2) (2017) 2791–2798.

[25] R. Engelke, J. Bdzil, A study of the steady-state reaction-zone structure of a homogeneous and a heterogeneous explosive, Phys. Fluids 26 (5) (1983) 1210–1221.

[26] W. C. Davis, T. R. Salyer, S. I. Jackson, T. D. Aslam, Explosive-driven shock waves in argon, in: Proceedings of the 13th International Detonation Symposium, Office of Naval Research, 1035–1044, 2006.

[27] G. Rodriguez, S. Gilbertson, S. W. Vincent, S. I. Jackson, Fiber Bragg grating sensors and their sensitivity to changes in detonation velocity across interfaces, in: Proceedings of the 15th International Detonation Symposium, Office of Naval Research, 264–272, 2015.

[28] A. W. Campbell, R. Engelke, The diameter effect in high-density heterogeneous explosives, in: Proceedings of the 6th International Detonation Symposium, Office of Naval Research, 642–652, 1976.

[29] L. G. Hill, J. B. Bdzil, W. C. Davis, R. R. Critchfield, PBX 9502 front curvature ratestick data: repeatability and the effects of temperature and material variation, in: Proceedings of the 13th International Detonation Symposium, Office of Naval Research, 351–07, 2006.

[30] C. Chiquete, M. Short, E. K. Anderson, S. I. Jackson, Detonation shock dynamics modeling and calibration of the HMX-based conventional high explosive PBX 9501 with application to the two-dimensional circular arc geometry, Combust. Flame 222 (2020) 213–232.

[31] S. Pemberton, T. Sandoval, T. Herrera, J. Echave, G. Maskaly, Test Report for Equation of State Measurements of PBX-9501, Tech. Rep. LA-UR-11-04999, Los Alamos National Laboratory, Los Alamos, NM, USA, 2011.

[32] S. Pemberton, T. Sandoval, T. Herrera, J. Echave, Test Report for Equation of State Measurements of PBX-9502, Tech. Rep. LA-UR-11-04998, Los Alamos National Laboratory, Los Alamos, NM, USA, 2011.

[33] J. A. Nelder, R. Mead, A simplex method for function minimization, Comput. J. 7 (4) (1965) 308–313.

[34] T. D. Aslam, J. B. Bdzil, D. S. Stewart, Level set methods applied to modeling detonation shock dynamics, J. Comput. Phys. 126 (2) (1996) 390–409.

[35] J. W. Kury, H. C. Hornig, E. L. Lee, J. L. McDonnel, D. L. Ornellas, M. Finger, F. M. Strange, M. L. Wilkins, Metal acceleration by chemical explosives, in: Proceedings of the 4th International Detonation Symposium, Office of Naval Research, 3–13, 1965.

[36] C. Mortensen, P. C. Souers, Optimizing code calibration of the JWL explosive equation-of-state to the cylinder test, Prop. Expl. Pyro. 42 (6) (2017) 616–622.

[37] C. Chiquete, S. I. Jackson, Detonation Performance of the CL-20-based Explosive LX-19, Proc. Combust. Inst. To Appear.

[38] J. H. Peterson, K. G. Honnell, C. Greeff, J. D. Johnson, J. Boettger, S. Crockett, Global equation of state for copper, in: AIP Conference Proceedings, vol. 1426, AIP, 763–766, 2012.

[39] D. L. Preston, D. L. Tonks, D. C. Wallace, Model of plastic deformation for extreme loading conditions, J. Appl. Phys. 93 (1) (2003) 211–220.

[40] D. E. Burton, Multidimensional discretization of conservation laws for unstructured polyhedral grids, Tech. Rep. UCRL-JC-118306, Lawrence Livermore National Laboratory, Livermore, CA, USA, 1994.

[41] E. J. Caramana, D. E. Burton, M. J. Shashkov, P. P. Whalen, The construction of compatible hydrodynamics algorithms utilizing conservation of total energy, J. Comput. Phys. 146 (1) (1998) 227–262.

[42] L. E. Fried, CHEETAH 1.0 users manual, Tech. Rep. UCRL-MA-117541, Lawrence Livermore National Laboratory, Livermore, CA, USA, 1994.

[43] D. S. Stewart, S. Yoo, W. C. Davis, Equation of state for modeling the detonation reaction zone, in: Proceedings of the 12th International Detonation Sympsium, Office of Naval Research, 1–11, 2002.

[44] D. E. Lambert, D. S. Stewart, S. Yoo, B. L. Wescott, Experimental validation of detonation shock dynamics in condensed explosives, J. Fluid Mech. 546 (2006) 227–253.

[45] M. J. Burns, C. Chiquete, Shock initiation of the HMX-based explosive PBX 9012: Experiments, uncertainty analysis, and unreacted equation-of-state, J. Appl. Phys. 127 (21) (2020) 215107.

[46] N. Desbiens, C. Matignon, R. Sorin, Temperature-based model for condensed-phase explosive detonation, in: Journal of Physics: Conference Series, vol. 500, IOP Publishing, 2014.

[47] C. Matignon, N. Desbiens, R. Sorin, V. Dubois, Theoretical study of the influence of the equation of state mixture properties on the velocitycurvature relationship for heterogeneous solid explosives, in: AIP Conference Proceedings, vol. 1426, AIP, 319–322, 2012.

[48] M. Short, C. Chiquete, J. B. Bdzil, J. J. Quirk, Detonation diffraction in a circular arc geometry of the insensitive high explosive PBX 9502, Combust. Flame (2018) 1–33.

[49] M. Short, E. K. Anderson, C. Chiquete, S. I. Jackson, Experimental and Modeling Analysis of Detonation in Circular Arcs of the Conventional High Explosive PBX 9501, Proc. Combust. Inst. To Appear.

[50] L. G. Hill, R. L. Gustavsen, R. R. Alcon, S. A. Sheffield, Shock initiation of new and aged PBX 9501 measured with embedded electromagnetic particle velocity gauges, Tech. Rep., Los Alamos National Laboratory, Los Alamos, NM, USA, 1999.

[51] R. L. Gustavsen, S. A. Sheffield, R. R. Alcon, Measurements of shock initiation in the tri-amino-tri-nitro-benzene based explosive PBX 9502: Wave forms from embedded gauges and comparison of four different material lots, J. Appl. Phys. 99 (11) (2006) 114907.

Appendix A. WSD Equations Appendix

Appendix A.1. WSD Reactants EOS

In the following, note that the state quantities having a subscript "0" refer to reference values for the subject HE which are typically correspond to ambient conditions at standard pressure and temperature. Also, note that temperature forms are not necessary for the use of the $p - \rho$ closure.

The state functions for the reactants (with subscript R) for the Davis reactants form can be stated as follows

$$e_R(p_R, v_R) = e_R^s(v_R) + \frac{v}{\Gamma_R(v_R)}(p_R - p_R^s(v_R)), \tag{A.1}$$

$$p_R(e_R, v_R) = p_R^s(v_R) + \frac{\Gamma_R(v_R)}{v_R}(e_R - e_R^s(v_R)), \tag{A.2}$$

where the specific volume v is such that $v = 1/\rho$, T is temperature and Grüneisen gamma and isentrope reference functions (defined in a piecewise continuous fashion):

$$\Gamma_R(v_R) = \begin{cases} \Gamma_R^0 + Zy, v_R \leq v_0 \\ \Gamma_R^0, v_R > v_0 \end{cases} \tag{A.3}$$

$$p_R^s(v_R) = \begin{cases} \hat{p}\left[C\dfrac{(4By)^4}{4!} + \dfrac{y^2}{(1-y)^4} + \displaystyle\sum_{j=1}^{3}\dfrac{(4By)^j}{j!}\right], \\ \qquad\qquad v_R \leq v_0 \\ \hat{p}(\exp(4By) - 1), v_R > v_0 \end{cases} \tag{A.4}$$

$$e_R^s(v_R) = \begin{cases} \frac{1}{\rho_0}\int_0^y p_R^s(y')dy' + E_{det}, v_R \leq v_0 \\ \frac{\hat{p}}{4B\rho_0}(\exp(4By) - 1 - 4By) + E_{det}, v_R > v_0 \end{cases} \tag{A.5}$$

where

$$y = 1 - v_R/v_0, \hat{p} = \rho_0 A^2/4B. \tag{A.6}$$

Here, the parameters A, B, C, Γ_R^0 and Z define an instance of the Davis reactant EOS. The reference internal energy E_{det} sets the energy released by reaction completion.

Appendix A.2. WSD Product EOS

Products. The corresponding Davis products form state quantities are as follows (denoted now by subscript P):

$$e_P(p_P, v_P) = e_P^s(v_P) + \frac{v_P}{\Gamma_P(v_P)}(p_P - p_P^s(v_P)), \tag{A.7}$$

$$p_P(e_P, v_P) = p_P^s(v_P) + \frac{\Gamma_P(v_P)}{v_P}(e_P - e_P^s(v_P)), \tag{A.8}$$

with isentrope reference quantities and Grüneisen gamma,

$$p_P^s(v_P) = p_c \frac{\left[\frac{1}{2}(v_P/v_c)^n + \frac{1}{2}(v_P/v_c)^{-n}\right]^{a/n}}{(v_P/v_c)^{k+a}} \frac{k-1+F(v_P)}{k-1+a} \tag{A.9}$$

$$e_P^s(v_P) = e_c \frac{\left[\frac{1}{2}(v_P/v_c)^n + \frac{1}{2}(v_P/v_c)^{-n}\right]^{a/n}}{(v_P/v_c)^{k-1+a}}, \tag{A.10}$$

$$\Gamma_p(v_P) = k - 1 + (1-b)F(v_P), \tag{A.11}$$

where

$$F(v_P) = \frac{2a(v_P/v_c)^{-n}}{(v_P/v_c)^n + (v_P/v_c)^{-n}}, e_c = \frac{p_c v_c}{k-1+a}, \tag{A.12}$$

Here, parameters p_c, v_c, a, k, n, b and the thermal parameter C_v define the products EOS parameters.

Appendix A.3. WSD Reaction Rate

To represent the finite rate of conversion, a WSD rate [6] was used,

$$\Lambda(\rho, p, \lambda, \rho_s) = r_I S_I + r_{IG} W S_G r_{DG}(1-W) S_G + r_B(1-S_G), \tag{A.13}$$

where the 4 sequential components are: ignition (r_I), ignition growth (r_{IG}), detonation growth (r_{DG}), and burnout (r_B), with functional dependencies,

$$r_I = k_I(1-\lambda)^b H((\rho/\rho_0 - 1 - a_I)^{n_I}), \tag{A.14}$$

$$r_{IG} = k_{IG}(1-\lambda)^c \lambda^d p^{n_{IG}}, \tag{A.15}$$

$$r_{DG} = k_{DG}(1-\lambda)^c \lambda^d p^{n_{DG}}, \tag{A.16}$$

$$r_B = k_B(1-\lambda)^e p^{n_B}, \tag{A.17}$$

Additionally, H is the Heaviside function and S_I, W and S_G are smooth blending terms,

$$S_I = \frac{1}{2}\Bigg(1 - \tanh(200(\lambda - 0.025))\Bigg), \tag{A.18}$$

$$W = \frac{1}{2}\Bigg(1 - \tanh\left(50\left(\frac{\rho_s}{\rho_c} - 1\right)\right)\Bigg), \tag{A.19}$$

$$S_G = \frac{1}{2}\Bigg(1 - \tanh(30(\lambda - \lambda_S))\Bigg). \tag{A.20}$$

PBX 9701 detonation performance data supplement

Carlos Chiquete, Scott I. Jackson, Eric K. Anderson, and Mark Short

Los Alamos National Laboratory
Los Alamos, NM 87545 USA

Abstract

The detonation performance data reported in the accompanying paper is presented including pellet densities, time-of-arrival and front shape measurements from the ratestick and CYLEX tests. Additionally, the CYLEX copper wall motion obtained from the 4 PDV probes is included.

1. Experimental Data Appendix

Table 1: Individual PBX 9701 pellet densities with pellet number increasing from the detonator side. Density tolerances are $\pm$ 0.001 g/cc. Average density is reported for pellets 3-12, which spanned the D_0 measurement length.

Pellet	8-1887	8-1895	8-1896	8-1897	8-1905
1	1.697	1.692	1.692	1.693	1.692
2	1.697	1.692	1.692	1.693	1.692
3	1.697	1.692	1.692	1.694	1.692
4	1.696	1.692	1.692	1.694	1.692
5	1.696	1.693	1.692	1.694	1.692
6	1.696	1.693	1.692	1.694	1.692
7	1.696	1.693	1.692	1.695	1.692
8	1.696	1.693	1.692	1.695	1.693
9	1.696	1.693	1.693	1.696	1.693
10	1.696	1.693	1.693	1.699	1.693
11	1.696	1.693	1.693	1.699	1.693
12	1.696	1.693	1.693	1.699	1.693
Avg.	1.696	1.693	1.692	1.696	1.693

1.1. Detonation Time of Arrival Data

8-1887 ionization data with x in mm and t in μs:
z = (0., 23.22, 46.2655, 69.277, 92.655, 115.683, 138.564, 161.855, 185.038, 208.051, 231.211)
t = (10.2793, 13.1748, 16.0645, 18.9581, 21.9031, 24.8101, 27.6907, 30.6412, 33.5621, 36.4675, 39.3942)

8-1895 ionization data with x in mm and t in μs:
z = (18.86, 27.5405, 36.151, 44.8975, 53.726, 62.2195, 70.9915, 79.454, 88.0715, 96.7065, 105.459)
t = (0., 1.1001 ,2.1887, 3.3007, 4.4199, 5.5002, 6.61197, 7.6875, 8.7833, 9.8724, 10.9912)

8-1896 ionization data with x in mm and t in μs:
z = (13.4115, 19.2835, 25.0285, 30.765, 36.4105, 42.381, 48.122, 53.79,59.634, 65.442, 71.0315)
t = (0.00015, 0.7457, 1.47157, 2.20563, 2.9223, 3.6841, 4.41565, 5.13883, 5.88603, 6.62463, 7.3293)

8-1897 ionization data with x in mm and t in μs:
z = (13.1095, 18.997, 24.545, 30.281, 36.2095, 41.8875, 47.765, 53.383, 59.156, 65.0235, 70.701)
t = (5.43646, 6.18693, 6.88571, 7.61573, 8.37086, 9.09026, 9.84016, 10.5549, 11.2925, 12.0415, 12.7574)

8-1905 ionization data with x in mm and t in μs:
z = (0, 23.1105, 46.132, 69.077, 92.308, 115.421, 138.463, 161.597, 184.66, 207.5, 230.92)
t = (10.8467, 13.7384, 16.6295, 19.5418, 22.4612, 25.3869, 28.2966, 31.2177, 34.1329, 36.9964, 39.9747)

1.2. Detonation Front Shape Data

8-1887 front shape data in mm:
r = (-12.9256, -12.9064, -12.8651, -12.7936, -12.7358, -12.667, -12.5899, -12.5101, -12.3973, -12.2845, -12.1689, -12.0644, -11.9213, -11.7975, -11.6379, -11.4425, -11.2884, -11.1536, -11.016, -10.8784, -10.7381, -10.595, -10.4492, -10.3254, -10.0915, -9.87686, -9.70901, -9.56318, -9.42285, -9.27976, -9.15869, -9.05138, -8.91655, -8.7322, -8.5671,

-8.41576, -8.26993, -8.15986, -8.03329, -7.87095, -7.7086, -7.49948, -7.32063, -7.15828, -7.02345, -6.85836, -6.72078, -6.56669, -6.42911, -6.28878, -6.14569, -6.02187, -5.85402, -5.7247, -5.57611, -5.36424, -5.07257, -4.80016, -4.53601, -4.31038, -4.05448, -3.8371, -3.661, -3.4904, -3.31155, -3.18773, -2.90156, -2.68143, -2.46956, -2.29346, -2.0293, -1.78441, -1.60556, -1.41019, -1.2451, -1.09376, -0.906652, -0.686524, 0.268281, 0.50767, 0.785581, 0.991951, 1.24785, 1.4267, 1.63582, 1.87246, 2.07333, 2.40352, 2.69244, 2.99236, 3.28678, 3.51241, 3.7518, 3.95267, 4.26635, 4.54977, 4.89372, 5.11109, 5.43853, 5.69994, 5.92832, 6.2365, 6.5034, 6.77856, 7.05372, 7.33714, 7.58203, 7.82142, 8.06631, 8.27818, 8.47355, 8.71569, 8.99085, 9.27426, 9.51915, 9.79982, 10.031, 10.2538, 10.4574, 10.6501, 10.7629, 10.9225, 11.0628, 11.1976, 11.3049, 11.4205, 11.5306, 11.6324, 11.759, 11.9681, 12.1442, 12.3038, 12.4331, 12.5294, 12.6202, 12.6972, 12.7633, 12.8238, 12.8871, 12.9256)

z= (0.86093, 0.816308, 0.776937, 0.732315, 0.692943, 0.661446, 0.648322, 0.629949, 0.6142, 0.587952, 0.577453, 0.566954, 0.545955, 0.530207, 0.514458, 0.496085, 0.475086, 0.459338, 0.443589, 0.435714, 0.425215, 0.406842, 0.404217, 0.37272, 0.36222, 0.341222, 0.328098, 0.320224, 0.314974, 0.3071, 0.304475, 0.293976, 0.283477, 0.267728, 0.254604, 0.244105, 0.236231, 0.228356, 0.230981, 0.220482, 0.215232, 0.196859, 0.183735, 0.178485, 0.178485, 0.165362, 0.162737, 0.157487, 0.152238, 0.149613, 0.149613, 0.141738, 0.133864, 0.123365, 0.112866, 0.104991, 0.0997419, 0.0839931, 0.0787436, 0.0761188, 0.0629949, 0.0551205, 0.0524957, 0.0498709, 0.0419966, 0.0314974, 0.0314974, 0.0288726, 0.0131239, 0.0131239, 0.00787436, 0.00524957, 0.00787436, 0.00787436, 0., 0.00524957, 0.00787436, 0.00524957, 0., 0.00524957, 0.00787436, 0.00787436, 0.00262479, 0.0104991, 0.0131239, 0.0131239, 0.0104991, 0.0131239, 0.0157487, 0.0104991, 0.0131239, 0.0209983, 0.0236231, 0.0341222, 0.0446214, 0.0446214, 0.0551205, 0.0551205, 0.073494, 0.073494, 0.0813684, 0.0971171, 0.107616, 0.12074, 0.139114, 0.144363, 0.154862, 0.170611, 0.18636, 0.202109, 0.217857, 0.223107, 0.244105, 0.267728, 0.270353, 0.296601, 0.3071, 0.338597, 0.349097, 0.364845, 0.370095, 0.380594, 0.388468, 0.401592, 0.406842, 0.42784, 0.443589, 0.451463, 0.454088, 0.475086, 0.509208, 0.530207, 0.551205, 0.587952, 0.590577, 0.66932, 0.761188, 0.842556, 0.963296, 1.06041)

8-1895 front shape data in mm:

r = (-5.1712, -5.15726, -5.13549, -5.11022, -5.07624, -5.04749, -5.02397, -4.98477, -4.96038, -4.94818, -4.92379, -4.89939, -4.87587, -4.84973, -4.82011, -4.79311, -4.76, -4.73299, -4.7025, -4.67027, -4.61451, -4.56398, -4.52652, -4.47686, -4.43591, -4.38626, -4.35489, -4.30175, -4.25993, -4.21637, -4.16671, -4.11836, -4.04431, -3.98071, -3.93628, -3.88488, -3.82825, -3.78557, -3.74201, -3.70629, -3.65402, -3.60436, -3.56515, -3.53205, -3.47629, -3.42751, -3.3822, -3.3295, -3.26328, -3.18749, -3.11518, -3.05855, -2.98973, -2.91306, -2.85818, -2.79632, -2.73185, -2.68917, -2.6308, -2.58157, -2.52582, -2.46396, -2.40733, -2.35245, -2.30802, -2.25749, -2.20783, -2.15469, -2.112, -2.06234, -2.01965, -1.97348, -1.93166, -1.87852, -1.82363, -1.76831, -1.68729, -1.62544, -1.56445, -1.50695,

-1.45729, -1.40067, -1.35101, -1.28218, -1.22991, -1.18287, -1.14018, -1.09488, -1.03912, -0.990333, -0.936318, -0.855297, -0.77776, -0.703708, -0.626172, -0.559961, -0.502462, -0.445835, -0.382237, -0.316897, 0.187526, 0.245895, 0.30078, 0.348697, 0.408809, 0.456725, 0.507254, 0.576079, 0.623995, 0.684978, 0.746834, 0.844407, 0.899292, 0.94808, 1.00384, 1.05001, 1.10925, 1.17459, 1.24864, 1.2983, 1.37584, 1.45425, 1.51436, 1.58057, 1.62848, 1.67989, 1.74, 1.80969, 1.87329, 1.92469, 1.9848, 2.03272, 2.08586, 2.13901, 2.18692, 2.23309, 2.30628, 2.36465, 2.44392, 2.52233, 2.57983, 2.66608, 2.72009, 2.7985, 2.85687, 2.91786, 2.97274, 3.04069, 3.11213, 3.19402, 3.26285, 3.3369, 3.41705, 3.49938, 3.57082, 3.63964, 3.71108, 3.79036, 3.86528, 3.9463, 4.01164, 4.08918, 4.16933, 4.23293, 4.30524, 4.37319, 4.44201, 4.51084, 4.54481, 4.59621, 4.6389, 4.68508, 4.72864, 4.77046, 4.80095, 4.82708, 4.87151, 4.90549, 4.95253, 4.98651, 5.00306, 5.03181, 5.06143, 5.08409, 5.11371, 5.1381, 5.1712)

z= (0.689714, 0.637594, 0.597634, 0.555939, 0.526405, 0.514243, 0.519455, 0.515982, 0.488184, 0.456912, 0.434329, 0.415217, 0.396107, 0.383945, 0.385683, 0.387421, 0.371786, 0.352673, 0.33009, 0.328352, 0.312716, 0.298818, 0.291868, 0.288395, 0.281444, 0.272759, 0.272759, 0.271021, 0.257123, 0.250173, 0.246699, 0.238011, 0.229325, 0.224113, 0.220639, 0.217163, 0.199792, 0.192842, 0.189368, 0.18763, 0.184156, 0.18068, 0.173732, 0.171994, 0.171994, 0.170256, 0.16852, 0.163308, 0.16157, 0.158096, 0.14246, 0.137248, 0.132037, 0.130298, 0.125086, 0.121613, 0.114663, 0.116401, 0.109451, 0.111189, 0.109451, 0.102501, 0.095553, 0.0938148, 0.0920766, 0.0886029, 0.0868647, 0.0851291, 0.0851291, 0.0816528, 0.0729671, 0.0694933, 0.0712289, 0.0712289, 0.0677551, 0.0694933, 0.0677551, 0.0694933, 0.0642814, 0.0538575, 0.0521193, 0.0521193, 0.0503812, 0.0434337, 0.0434337, 0.0469074, 0.0451692, 0.0382217, 0.0347454, 0.0330098, 0.0295334, 0.0260597, 0.0243215, 0.0243215, 0.0225859, 0.0208477, 0.0208477, 0.017374, 0.0208477, 0.012162, 0.00695011, 0.00868569, 0.00521193, 0.00695011, 0.00521193, 0., 0.00173818, 0.00868569, 0.00868569, 0.00695011, 0.0104239, 0.00347375, 0.00695011, 0.00868569, 0.00347375, 0., 0.00347375, 0.0078179, 0.0078179, 0.00607972, 0.00260597, 0.00434415, 0.0078179, 0.0078179, 0.00955608, 0.00955608, 0.00607972, 0.00607972, 0.00955608, 0.00955608, 0.00955608, 0.0078179, 0.00955608, 0.0112917, 0.0112917, 0.0208477, 0.0225859, 0.0295334, 0.0312716, 0.0312716, 0.0347454, 0.0312716, 0.0330098, 0.0399573, 0.0347454, 0.0312716, 0.0399573, 0.0434337, 0.0469074, 0.0521193, 0.0503812, 0.0555931, 0.0642814, 0.0729671, 0.0747053, 0.0677551, 0.0729671, 0.0799172, 0.0868647, 0.0886029, 0.0990268, 0.107712, 0.111189, 0.126825, 0.125086, 0.12856, 0.138984, 0.145934, 0.156358, 0.170256, 0.185891, 0.206739, 0.225851, 0.251911, 0.272759, 0.298818, 0.328352, 0.328352, 0.331826, 0.370047, 0.410005, 0.470812, 0.512508, 0.581998, 0.654966, 0.733145, 0.825224)

8-1897 front shape data in mm:

r = (-3.39242, -3.37494, -3.34945, -3.32832, -3.30429, -3.28244, -3.25549, -3.23291, -3.20814, -3.18046, -3.1455, -3.11928, -3.08504, -3.05373, -3.01876, -2.98453, -2.95539, -2.92116, -2.88547, -2.85269, -2.81992, -2.77476, -2.74416, -2.72158, -2.68371, -2.65822,

-2.62981, -2.60504, -2.57591, -2.54386, -2.5089, -2.47175, -2.43242, -2.38799, -2.33263, -2.27946, -2.24158, -2.20298, -2.1651, -2.13233, -2.1021, -2.06131, -2.02271, -1.96589, -1.91345, -1.85445, -1.80055, -1.74082, -1.67964, -1.62792, -1.58131, -1.52522, -1.46258, -1.41815, -1.37226, -1.32128, -1.26009, -1.19891, -1.14865, -1.09475, -1.04304, -0.984767, -0.917028, -0.838363, -0.765525, -0.689045, -0.620578, -0.531715, -0.426101, 0.150774, 0.201761, 0.2695, 0.328499, 0.421003, 0.494569, 0.578697, 0.661732, 0.752051, 0.833629, 0.918121, 0.988773, 1.0638, 1.14392, 1.21311, 1.29797, 1.37736, 1.46695, 1.5733, 1.66143, 1.73864, 1.8122, 1.8865, 1.93931, 2.01724, 2.08353, 2.14034, 2.19788, 2.25761, 2.29476, 2.33846, 2.37815, 2.41894, 2.47794, 2.59958, 2.66878, 2.73506, 2.80498, 2.872, 2.91133, 2.94702, 2.98052, 3.01804, 3.06028, 3.10471, 3.1455, 3.18775, 3.22635, 3.25986, 3.28462, 3.31594, 3.34362, 3.36984, 3.3924)
z= (0.551282, 0.527012, 0.492339, 0.457668, 0.416062, 0.391792, 0.362319, 0.334584, 0.305111, 0.282576, 0.266974, 0.260038, 0.244436, 0.230568, 0.223633, 0.211497, 0.211497, 0.204564, 0.192428, 0.183761, 0.180292, 0.178561, 0.175092, 0.171625, 0.168159, 0.161224, 0.159489, 0.156023, 0.156023, 0.147356, 0.142155, 0.138686, 0.13522, 0.130019, 0.119618, 0.116151, 0.107482, 0.10575, 0.102281, 0.102281, 0.104015, 0.100549, 0.0970802, 0.0901475, 0.0849468, 0.0780115, 0.0728108, 0.0745452, 0.06761, 0.0606748, 0.0589429, 0.0589429, 0.0502732, 0.0520077, 0.0537421, 0.0468069, 0.0468069, 0.0364054, 0.0329391, 0.0312046, 0.0329391, 0.0294702, 0.0242694, 0.0156023, 0.0138679, 0.0138679, 0.0138679, 0.0104015, 0.0104015, 0.00520077, 0.00693523, 0.00520077, 0.00346631, 0.00173446, 0., 0.0060667, 0.000865928, 0.0060667, 0.00780115, 0.000865928, 0.00433484, 0.0112675, 0.00780115, 0.0112675, 0.0138679, 0.0208031, 0.0156023, 0.0277383, 0.0260038, 0.0294702, 0.0398717, 0.0398717, 0.0442065, 0.0407402, 0.0476728, 0.0546081, 0.0632752, 0.0650096, 0.0650096, 0.0702104, 0.0702104, 0.0754112, 0.0840782, 0.0927479, 0.106616, 0.110082, 0.113551, 0.123953, 0.130885, 0.143021, 0.148222, 0.151688, 0.158623, 0.184627, 0.215832, 0.250503, 0.293843, 0.34065, 0.368389, 0.415196, 0.451601, 0.496673, 0.541746)

8-1905 front shape data in mm:
r = (-12.5722, -12.5172, -12.4491, -12.3652, -12.2708, -12.1686, -12.0454, -11.9275, -11.82, -11.6995, -11.5763, -11.4662, -11.3247, -11.1779, -10.9971, -10.7612, -10.5542, -10.355, -10.1663, -9.954, -9.73909, -9.50059, -9.29879, -9.07601, -8.87421, -8.75889, -8.46273, -8.22162, -8.01457, -7.81538, -7.60834, -7.4406, -7.30694, -7.06582, -6.81946, -6.58096, -6.30839, -6.04106, -5.85236, -5.60338, -5.33606, -5.10542, -4.7883, -4.51835, -4.26413, -3.98632, -3.80155, -3.59712, -3.33503, -3.11226, -2.85804, -2.66409, -2.47278, -2.3129, -2.08227, -1.8228, -1.64982, -1.39036, -0.841294, -0.600173, -0.264705, 0.0104847, 0.33285, 0.629005, 0.838676, 1.14793, 1.50699, 1.80577, 2.14124, 2.42953, 2.71258, 3.02709, 3.318, 3.67706, 3.91555, 4.19861, 4.40303, 4.6245, 4.92852, 5.24302, 5.47103, 5.75671, 6.01879, 6.24943, 6.44075, 6.70283, 6.94133, 7.17197, 7.38163, 7.61489, 7.85208, 8.04864, 8.24783, 8.49681, 8.75627, 9.0236, 9.28044, 9.49011, 9.7653, 10.0615, 10.3209, 10.5096, 10.7009, 10.8189, 10.963, 11.1177, 11.2828, 11.4164, 11.5344, 11.6445, 11.7493,

11.8122, 11.9118, 12.0166, 12.1241, 12.1686, 12.2866, 12.4019, 12.4884, 12.5565, 12.5722)
z= (0.68234, 0.675353, 0.668362, 0.65613, 0.645646, 0.621184, 0.607206, 0.59148, 0.572257, 0.561773, 0.553037, 0.533817, 0.518091, 0.507607, 0.491881, 0.462174, 0.442954, 0.425479, 0.414995, 0.394027, 0.378301, 0.364323, 0.343355, 0.32588, 0.318893, 0.313651, 0.289186, 0.27346, 0.262976, 0.250746, 0.236765, 0.23502, 0.222787, 0.210555, 0.194829, 0.180851, 0.165125, 0.159883, 0.152892, 0.142408, 0.131924, 0.12144, 0.114452, 0.100472, 0.091736, 0.0830001, 0.0760098, 0.0707678, 0.0585354, 0.0480513, 0.0463057, 0.0428093, 0.0358216, 0.0305795, 0.0270831, 0.016599, 0.0235893, 0.0253375, 0.0139779, 0.0122323, 0.0122323, 0.00873589, 0.00699028, 0., 0.00699028, 0.00524206, 0.00349383, 0.00524206, 0.00699028, 0.00699028, 0.0122323, 0.0139779, 0.0122323, 0.0157262, 0.0209682, 0.0314523, 0.0366944, 0.0419365, 0.0471785, 0.0576626, 0.0663985, 0.0716406, 0.0768826, 0.0786309, 0.089115, 0.0961053, 0.113577, 0.118819, 0.136293, 0.146778, 0.152892, 0.161631, 0.168619, 0.184345, 0.194829, 0.210555, 0.228029, 0.242007, 0.259482, 0.27346, 0.292682, 0.313651, 0.318893, 0.336364, 0.350345, 0.366071, 0.378301, 0.388785, 0.402766, 0.414995, 0.43247, 0.444702, 0.45868, 0.479648, 0.502365, 0.519836, 0.546047, 0.567015, 0.596722, 0.642152, 0.671856)

1.3. Cylinder Expansion Wall Motion Records

8-1905 PDV records with t in μs and v_r (wall velocity component normal to probe) in mm/μs:
(Probe azimuthal locations θ are reported relative to PDV 1)
PDV 1 at z = 152 mm and $\theta = 0°$:
t = (0., 0.03456, 0.08832, 0.15744, 0.21248, 0.23168, 0.27648, 0.29696, 0.36352, 0.39808, 0.42752, 0.45696, 0.48, 0.50176, 0.51456, 0.53248, 0.56192, 0.59008, 0.63104, 0.69376, 0.72192, 0.8768, 0.9664, 0.98176, 0.98688, 0.99328, 0.99968, 1.00352, 1.00864, 1.01632, 1.02272, 1.02784, 1.05728, 1.07264, 1.10208, 1.14048, 1.16736, 1.184, 1.18912, 1.1968, 1.20832, 1.21472, 1.22368, 1.23136, 1.2416, 1.28896, 1.3248, 1.36704, 1.42976, 1.49376, 1.52064, 1.5808, 1.59872, 1.61792, 1.66016, 1.70112, 1.72416, 1.73184, 1.74592, 1.76384, 1.78944, 1.83296, 1.8688, 1.87392, 1.90464, 1.92384, 1.96864, 1.984, 2.04544, 2.08768, 2.12608, 2.176, 2.19904, 2.2208, 2.24768, 2.30144, 2.39104, 2.43072, 2.46016, 2.49088, 2.53952, 2.59456, 2.688, 2.72896, 2.7776, 2.81088, 2.82624, 2.88768, 2.96448, 3.06304, 3.17824, 3.296, 3.38048, 3.43296, 3.4816, 3.50976, 3.59168, 3.66848, 3.712, 3.74912, 3.81696, 3.96416, 4.09728, 4.15744, 4.22272, 4.31616, 4.3904, 4.47488, 4.52992, 4.58112, 4.65536, 4.71808, 4.79616, 4.896, 4.91904, 4.96768, 5.1008, 5.2416, 5.35424, 5.44, 5.53728, 5.64352, 5.76512, 5.84192, 5.96992, 6.0288, 6.10432, 6.18752, 6.32704, 6.45248, 6.52672, 6.7328, 6.82752, 6.88128, 6.98368, 7.15264, 7.24608, 7.28576, 7.54176, 7.63008, 7.72864, 7.80032, 7.84896, 7.88864, 8.1536, 8.29696, 8.33536, 8.3904, 8.5696, 8.82816, 9.32224, 9.67168, 10.1184, 10.217, 10.4064, 10.592, 10.8352, 11.1821, 11.584, 11.7274, 11.8208, 11.9258, 12.1856, 12.4493, 12.5107, 12.6426, 12.8358, 13.0995, 13.5181, 13.6678,

13.7971, 13.9674, 14.2938, 14.4576, 14.5549, 15.0746, 15.9936, 16.6554, 16.9638, 17.1085, 17.3914, 17.7421, 18.4678, 18.9389, 19.1616, 19.4176, 19.4778, 19.6506, 19.7824, 19.936, 20.0909, 20.1677, 20.32, 20.5645, 20.7718, 20.8435, 21.0214, 21.2096, 21.335, 21.4848, 21.5782, 21.5872, 21.5885)

v_r= (0.889282, 0.773116, 0.756239, 0.737453, 0.740184, 0.737177, 0.718918, 0.700483, 0.68614, 0.66411, 0.644314, 0.638546, 0.639537, 0.659268, 0.67779, 0.684005, 0.691428, 0.693181, 0.694613, 0.690548, 0.678067, 0.66753, 0.681166, 0.698035, 0.716209, 0.740674, 0.752205, 0.765253, 0.790149, 0.816611, 0.822169, 0.852671, 0.87497, 0.894846, 0.912716, 0.928955, 0.949622, 0.945479, 0.96271, 0.985596, 0.985909, 0.969726, 0.990584, 1.00816, 1.02972, 1.03315, 1.01616, 1.00586, 0.996935, 0.982708, 0.970864, 0.966742, 0.974925, 0.959217, 0.962305, 0.950051, 0.944677, 0.966643, 0.971171, 0.945404, 0.960544, 0.972578, 0.989772, 1.00488, 1.02196, 1.04111, 1.05393, 1.06532, 1.07972, 1.1005, 1.12104, 1.12438, 1.13726, 1.14114, 1.1589, 1.15482, 1.14685, 1.13401, 1.13188, 1.12785, 1.1222, 1.1149, 1.11726, 1.1363, 1.15705, 1.17026, 1.1911, 1.20099, 1.211, 1.22222, 1.22876, 1.2328, 1.22606, 1.21918, 1.22743, 1.2062, 1.2264, 1.24227, 1.26223, 1.27859, 1.29625, 1.29512, 1.29028, 1.28867, 1.27869, 1.28553, 1.28447, 1.29614, 1.31281, 1.32727, 1.34302, 1.34118, 1.34451, 1.34105, 1.33713,

1.36099, 1.36518, 1.372, 1.3755, 1.37573, 1.3974, 1.40381, 1.39352, 1.39303, 1.4046, 1.41077, 1.41903, 1.42411, 1.42203, 1.41889, 1.41631, 1.43567, 1.43359, 1.44278, 1.43444, 1.43144, 1.43978, 1.45029, 1.45136, 1.4533, 1.45428, 1.45965, 1.46729, 1.47542, 1.47714, 1.48867, 1.49056, 1.49675, 1.49913, 1.50192, 1.50941, 1.51403, 1.51556, 1.5107, 1.5159, 1.52147, 1.52431, 1.52418, 1.52461, 1.52927, 1.53071, 1.53567, 1.53594, 1.53822, 1.5394, 1.54295, 1.54347, 1.54449, 1.55105, 1.55659, 1.56162, 1.56206, 1.56369, 1.56535, 1.56639, 1.56972, 1.57105, 1.57327, 1.57932, 1.58317, 1.57404, 1.57882, 1.57714, 1.57558, 1.57428, 1.57923, 1.58097, 1.57891, 1.57312, 1.57839, 1.57899, 1.57305, 1.58129, 1.58507, 1.58323, 1.58313)

PDV 2 at z = 152 mm and θ = 90°:

t = (0., 0.02176, 0.06784, 0.1216, 0.16384, 0.20864, 0.24832, 0.29952, 0.35072, 0.45568, 0.47872, 0.5184, 0.65664, 0.70016, 0.7552, 0.86912, 0.93952, 0.9664, 1.00224, 1.0048, 1.00864, 1.0112, 1.01888, 1.03552, 1.04704, 1.09952, 1.17632, 1.18528, 1.22112, 1.248, 1.3056, 1.35296, 1.4016, 1.45408, 1.50656, 1.55392, 1.64608, 1.72416, 1.77664, 1.81504, 1.8368, 1.856, 1.87008, 1.8752, 1.89568, 1.90464, 1.9136, 1.92512, 1.95328, 1.97632, 1.99808, 2.06336, 2.12224, 2.19776, 2.25408, 2.28352, 2.30528, 2.31296, 2.368, 2.42048, 2.46528, 2.52416, 2.60864, 2.67776, 2.70336, 2.74944, 2.78528, 2.80832, 2.84928, 2.87232, 2.92224, 2.96192, 3.05408, 3.09504, 3.15392, 3.19488, 3.26016, 3.29728, 3.33056, 3.37792, 3.38688, 3.40864, 3.45088, 3.47648, 3.51616, 3.55584, 3.58912, 3.63392, 3.69536, 3.74784, 3.78752, 3.82464, 3.9104, 4.00384, 4.04352, 4.1344, 4.17024, 4.22656, 4.28672, 4.34944, 4.40192, 4.4672, 4.50944, 4.55424, 4.61184, 4.65792, 4.6976, 4.75136, 4.80512, 4.9152, 5.01504, 5.08288, 5.1264, 5.18656, 5.30816, 5.3568, 5.51552, 5.65632, 5.728, 5.80224,

5.9136, 6.01856, 6.08128, 6.24, 6.42816, 6.48192, 6.51648, 6.65984, 6.7776, 6.89152, 7.13472, 7.40608, 7.73248, 8.06784, 8.29312, 8.59264, 8.69888, 9.1456, 9.57568, 9.82272, 10.24, 10.6573, 10.7725, 11.1053, 11.4432, 11.8758, 12.2893, 12.4096, 12.471, 12.5082, 12.5965, 12.8269, 13.1123, 13.1968, 13.4272, 13.7395, 13.8701, 13.9968, 14.2323, 14.4474, 14.8646, 15.3894, 15.7338, 15.9936, 16.3226, 16.6029, 16.9216, 17.1584, 17.6627, 17.8035, 17.856, 17.8701, 17.8906, 17.9366, 18.4397, 18.6765, 19.3037, 19.7555, 20.16, 20.6989, 20.7846, 21.1213, 21.3978, 21.7651, 21.9994, 22.2054, 22.3168, 22.4768, 22.9082, 23.159, 23.3626, 23.68, 23.7594, 23.7773, 23.7786)
v_r= (0.761336, 0.751429, 0.750915, 0.738139, 0.727847, 0.724751, 0.715195, 0.69916, 0.682401, 0.672034, 0.671502, 0.649375, 0.653304, 0.665068, 0.664974, 0.671638, 0.690208, 0.7056, 0.840174, 0.852958, 0.882436, 0.899019, 0.950326, 0.949217, 0.971045, 0.988836, 0.993375, 0.97829, 1.00043, 1.00493, 1.00932, 1.00545, 0.997905, 0.98261, 0.964386, 0.964457, 0.951578, 0.941298, 0.948975, 0.966169, 0.982816, 0.997368, 0.985244, 1.00491, 1.02777, 1.0471, 1.06478, 1.08819, 1.08173, 1.09958, 1.12109, 1.13871, 1.15579, 1.16042, 1.16477, 1.15685, 1.16974, 1.15085, 1.14887, 1.1316, 1.12694, 1.1264, 1.11113, 1.11839, 1.13201, 1.14236, 1.15851, 1.17747, 1.19205, 1.21221, 1.21844, 1.2386, 1.25063, 1.25138, 1.25948, 1.24812, 1.24049, 1.23827, 1.24209, 1.22923, 1.22354, 1.21548, 1.21236, 1.22294, 1.2187, 1.2202, 1.24105, 1.24899, 1.26716, 1.28268, 1.29163, 1.30634, 1.31553, 1.31219, 1.31443, 1.30303, 1.28971, 1.28744, 1.29393, 1.29257, 1.30844, 1.32014, 1.32728, 1.33366, 1.34142, 1.34, 1.34867, 1.35413, 1.34761, 1.34436, 1.34199, 1.34909, 1.33726, 1.35555, 1.36896, 1.37863, 1.38849, 1.37423, 1.37523, 1.37592, 1.39276, 1.40279, 1.40886, 1.41446, 1.41106, 1.40946, 1.41346, 1.42455, 1.43526, 1.433, 1.43304, 1.45122, 1.45157, 1.46887, 1.47479, 1.47736, 1.48089, 1.48884, 1.49458, 1.50217, 1.5079, 1.51421, 1.51699, 1.52184, 1.52723, 1.53104, 1.53577, 1.53807, 1.53502, 1.53665, 1.54151, 1.54318, 1.5477, 1.55234, 1.55096, 1.55396, 1.54498, 1.55663, 1.56077, 1.56214, 1.56649, 1.56871, 1.57665, 1.57615, 1.57872, 1.5802, 1.58269, 1.59053, 1.5866, 1.5832, 1.58177, 1.60458, 1.58039, 1.59131, 1.5938, 1.59241, 1.59255, 1.59507, 1.59384, 1.59575, 1.5941, 1.59246, 1.59594, 1.59608, 1.59454, 1.59127, 1.59742, 1.59665, 1.59751, 1.59484, 1.59419, 1.60374, 1.60317, 1.60091, 1.60095)

PDV 3 at z = 203 mm and θ = 270°:
t = (0., 0.02816, 0.06144, 0.08448, 0.11776, 0.14336, 0.17408, 0.20224, 0.24192, 0.28416, 0.31232, 0.35072, 0.3584, 0.3648, 0.3712, 0.39808, 0.43008, 0.49792, 0.54272, 0.56448, 0.61824, 0.66048, 0.6976, 0.75648, 0.83712, 0.91392, 0.96128, 0.99072, 0.99968, 1.00224, 1.00864, 1.01248, 1.01888, 1.0304, 1.03808, 1.04576, 1.05344, 1.0752, 1.08416, 1.1136, 1.12, 1.12256, 1.12512, 1.12768, 1.13664, 1.152, 1.1712, 1.20448, 1.2416, 1.25568, 1.26592, 1.31584, 1.36064, 1.37344, 1.3888, 1.4144, 1.4592, 1.47968, 1.49888, 1.53728, 1.60896, 1.63712, 1.66656, 1.6832, 1.7088, 1.73952, 1.75488, 1.792, 1.82912, 1.87392, 1.9008, 1.93792, 1.95712, 1.99168, 2.0416, 2.112, 2.21696, 2.3296, 2.42944, 2.47168, 2.60224, 2.6688, 2.72512, 2.76224, 2.81472, 2.86208, 2.91712, 3.00928, 3.11296, 3.18976,

3.21664, 3.27296, 3.34336, 3.38688, 3.41888, 3.4496, 3.50464, 3.5776, 3.66976, 3.7056, 3.74656, 3.81056, 3.9616, 4.06016, 4.13312, 4.1664, 4.21504, 4.33792, 4.38784, 4.45824, 4.49408, 4.53632, 4.60032, 4.65536, 4.704, 4.76928, 4.82176, 4.91904, 5.01248, 5.11488, 5.18656, 5.26464, 5.33376, 5.41056, 5.472, 5.60384, 5.68448, 5.79328, 5.9072, 6.00064, 6.0672, 6.1888, 6.3616, 6.5536, 6.62656, 6.71872, 6.816, 6.86208, 7.00032, 7.1552, 7.35488, 7.43808, 7.63008, 7.91424, 8.00128, 8.20736, 8.4544, 8.69632, 8.8512, 9.088, 9.26848, 9.54624, 9.89312, 10.4781, 10.8339, 11.1411, 11.6749, 12.169, 12.617, 13.5987, 13.952, 14.0339, 14.3078, 14.8339, 15.2166, 15.5584, 16.2022, 16.6182, 17.0893, 18.3373, 19.0912, 19.2666, 19.5686, 19.9757, 20.1946, 20.873, 21.321, 21.5398, 21.7958, 22.1235, 22.2963, 22.5318, 22.697, 22.8019, 22.9645, 23.2128, 23.3574, 23.5187, 23.6416, 23.6531, 23.6544)

v_r= (0.77552, 0.781396, 0.769022, 0.756494, 0.74652, 0.728616, 0.728154, 0.724112, 0.718168, 0.708302, 0.714869, 0.776336, 0.744732, 0.718938, 0.694268, 0.67863, 0.65874, 0.685094, 0.655321, 0.660331, 0.681351, 0.678067, 0.680507, 0.692509, 0.678238, 0.696403, 0.708787, 0.8092, 0.851963, 0.869871, 0.93165, 0.919709, 0.914774, 0.946522, 0.964182, 0.942784, 0.955144, 0.978076, 0.956689, 0.874979, 0.849626, 0.869506, 0.899047, 0.919885, 0.963058, 0.960541, 0.989966, 0.986133, 0.964248, 0.975745, 1.00466, 1.02062, 1.00891, 0.995369, 1.01085, 1.0055, 0.989743, 0.968197, 0.974369, 0.963201, 0.959713, 0.973624, 0.957212, 0.957545, 0.940074, 0.950838, 0.975205, 0.968557, 0.989582, 1.01412, 1.03944, 1.05835, 1.09245, 1.11483, 1.12876, 1.1524, 1.15643, 1.1514, 1.14463, 1.13735, 1.12668, 1.13268, 1.15437, 1.15583, 1.1813, 1.198, 1.22293, 1.24216, 1.25049, 1.24049, 1.23909, 1.24153, 1.22766, 1.23009, 1.2202, 1.2212, 1.22913, 1.24234, 1.26617, 1.27152, 1.28861, 1.30152, 1.31512, 1.30086, 1.2979, 1.29394, 1.29096, 1.2904, 1.29705, 1.32512, 1.32344, 1.33124, 1.34554, 1.35734, 1.35442, 1.36364, 1.36101, 1.34329, 1.33477, 1.34747, 1.35116, 1.36515, 1.37713, 1.38688, 1.38083, 1.38698, 1.37755, 1.37539, 1.38525, 1.39426, 1.40766, 1.41736, 1.41165, 1.40549, 1.41435, 1.42426, 1.43338, 1.43117, 1.43259, 1.43402, 1.43812, 1.44433, 1.45207, 1.45667, 1.45882, 1.46815, 1.4602, 1.47499, 1.48096, 1.47739, 1.48794, 1.49171, 1.50217, 1.50836, 1.51456, 1.51589, 1.52645, 1.53035, 1.53675, 1.54684, 1.55077, 1.54161, 1.5527, 1.55708, 1.5603, 1.56237, 1.56332, 1.56836, 1.572, 1.57814, 1.58712, 1.57944, 1.58505, 1.58036, 1.58833, 1.58823, 1.5959, 1.58962, 1.58976, 1.59369, 1.59152, 1.6012, 1.59779, 1.59682, 1.59799, 1.59626, 1.59634, 1.59761, 1.59528, 1.59504, 1.59536)

PDV 4 at z = 203 mm and θ = 180°:

t = (0., 0.04608, 0.1024, 0.14208, 0.18944, 0.22016, 0.23552, 0.31488, 0.37632, 0.48256, 0.5824, 0.66304, 0.7744, 0.8448, 0.8704, 0.89472, 0.93952, 0.9792, 0.99968, 1.00992, 1.01504, 1.0176, 1.02528, 1.0432, 1.06368, 1.09824, 1.11872, 1.16224, 1.16992, 1.24416, 1.32224, 1.37856, 1.38496, 1.41952, 1.42976, 1.47072, 1.51168, 1.58848, 1.65504, 1.68704, 1.72928, 1.75744, 1.79584, 1.84576, 1.87136, 1.88288, 1.91872, 1.952, 1.97504, 2.02752, 2.06208, 2.09664, 2.19648, 2.22848, 2.24, 2.2656, 2.31552, 2.38848, 2.4448, 2.49984, 2.54464, 2.57664, 2.6112, 2.68288, 2.70336, 2.7584, 2.8032, 2.82112, 2.85568, 2.89664,

2.92992, 2.944, 3.03488, 3.17952, 3.25248, 3.35616, 3.43936, 3.48416, 3.54688, 3.5904, 3.68256, 3.74784, 3.80928, 3.82976, 3.89888, 3.98976, 4.07808, 4.1088, 4.17536, 4.21376, 4.30208, 4.34432, 4.42752, 4.47616, 4.54272, 4.61952, 4.72832, 4.80128, 4.87424, 4.95104, 5.03808, 5.09824, 5.25312, 5.30176, 5.39264, 5.49376, 5.5488, 5.63456, 5.75232, 5.84064, 5.99168, 6.0544, 6.16064, 6.20672, 6.29504, 6.40384, 6.48704, 6.55616, 6.62016, 6.70208, 6.75456, 6.8352, 6.98624, 7.104, 7.15648, 7.296, 7.39456, 7.5136, 7.648, 7.80032, 7.95904, 8.19456, 8.41984, 8.6528, 8.75648, 8.85248, 9.0048, 9.216, 9.34784, 9.4144, 9.49376, 9.55136, 9.59744, 9.84832, 10.121, 10.2221, 10.3667, 10.4653, 10.5741, 10.7226, 10.8851, 11.0835, 11.2269, 11.351, 11.4278, 11.5226, 11.5814, 11.8566, 12.0422, 12.2957, 12.3699, 12.4557, 12.6054, 12.7923, 12.9971, 13.2262, 13.5334, 13.7728, 13.8458, 13.9597, 14.1747, 14.4166, 14.7955, 15.2538, 15.5891, 15.8234, 16.0128, 16.3494, 16.6515, 16.8013, 16.9088, 17.1584, 17.2954, 17.4835, 17.7395, 17.8445, 17.9968, 18.5178, 18.7866, 18.976, 19.1731, 19.1757, 19.177)

v_r= (0.779143, 0.769208, 0.765008, 0.741629, 0.731102, 0.788409, 0.720403, 0.699106, 0.681823, 0.668464, 0.675328, 0.683604, 0.678581, 0.671464, 0.675874, 0.691697, 0.697252, 0.715393, 0.776435, 0.759828, 0.79074, 0.805938, 0.877236, 0.966284, 0.992657, 1.00482, 1.00509, 0.963847, 0.989718, 1.00581, 1.00187, 0.996454, 0.996146, 0.999238, 0.982682, 1.00767, 0.982696, 0.972041, 0.950773, 0.960484, 0.954854, 0.972572, 0.968655, 1.00142, 1.02732, 1.05482, 1.06073, 1.08756, 1.10311, 1.1219, 1.12932, 1.15332, 1.1521, 1.13264, 1.13862, 1.13768, 1.15658, 1.14608, 1.13928, 1.13555, 1.13406, 1.13426, 1.12429, 1.14031, 1.14345, 1.18243, 1.18263, 1.17722, 1.21219, 1.21562, 1.19943, 1.22952, 1.24755, 1.24923, 1.25025, 1.23034, 1.23893, 1.22411, 1.23838, 1.26135, 1.28089, 1.29386, 1.29694, 1.3065, 1.3067, 1.30601, 1.30467, 1.30303, 1.29661, 1.28532, 1.29878, 1.31334, 1.32868, 1.33798, 1.34743, 1.35356, 1.35511, 1.35792, 1.35946, 1.34301, 1.34294, 1.35402, 1.37296, 1.38833, 1.38993, 1.39685, 1.399, 1.38546, 1.38385, 1.39103, 1.41483, 1.41842, 1.42849, 1.43284, 1.41333, 1.41581, 1.41433, 1.41159, 1.42466, 1.43568, 1.44003, 1.44476, 1.44536, 1.43797, 1.4382, 1.44473, 1.45835, 1.46436, 1.46569, 1.44945, 1.46895, 1.48008, 1.48285, 1.48911, 1.49573, 1.49569, 1.49389, 1.5041, 1.5055, 1.50309, 1.49329, 1.50704, 1.50192, 1.51408, 1.51567, 1.51687, 1.52198, 1.52314, 1.52144, 1.52638, 1.53287, 1.53458, 1.53363, 1.54016, 1.53856, 1.5418, 1.53615, 1.5458, 1.54786, 1.55032, 1.55593, 1.55342, 1.55144, 1.55579, 1.56109, 1.56392, 1.56431, 1.56451, 1.56552, 1.5653, 1.57079, 1.5723, 1.57475, 1.57818, 1.57833, 1.58026, 1.58363, 1.58543, 1.58504, 1.58557, 1.5864, 1.58964, 1.59038, 1.59182, 1.59586, 1.59891, 1.5948, 1.59759, 1.59845, 1.59893, 1.602, 1.60246, 1.60262)